

# Reducing uncertainty in local climate projections

Saïd Qasmi (✉ [said.qasmi@meteo.fr](mailto:said.qasmi@meteo.fr))

Centre National de Recherches Météorologiques <https://orcid.org/0000-0002-1825-3896>

Aurélien Ribes

Centre National de Recherches Météorologiques <https://orcid.org/0000-0001-5102-7885>

---

## Article

**Keywords:** climate change, climate projections, adaptation, temperature

**Posted Date:** February 7th, 2022

**DOI:** <https://doi.org/10.21203/rs.3.rs-364943/v2>

**License:**  This work is licensed under a Creative Commons Attribution 4.0 International License.

[Read Full License](#)

---

1                   **Reducing uncertainty in local climate projections**

2                                   Saïd Qasmi,<sup>a</sup> Aurélien Ribes<sup>a</sup>

3                   <sup>a</sup> *CNRM, Université de Toulouse, Météo-France, CNRS, Toulouse, France*

4   *Corresponding author: Saïd Qasmi, [said.qasmi@umr-cnrm.fr](mailto:said.qasmi@umr-cnrm.fr)*

5 ABSTRACT: Planning for adaptation to climate change requires accurate climate projections.  
6 Recent studies have shown that the uncertainty in global mean surface temperature projections can  
7 be considerably reduced by using historical observations. However, the transposition of these new  
8 results to the local scale is not yet available. We adapt an innovative statistical method that combines  
9 the latest generation of climate model simulations, global observations, and local observations to  
10 reduce uncertainty in local temperature projections. By taking advantage of the tight links between  
11 local and global temperature, we can derive the local implications of global constraints. The model  
12 uncertainty is reduced by 30% up to 50% at any location worldwide, allowing to substantially  
13 improve the quantification of risks associated with future climate change. A rigorous evaluation of  
14 these results within a perfect model framework indicates a robust skill, leading to a high confidence  
15 in our constrained climate projections.

## 16 **1. Introduction**

17 As the global mean temperature keeps rising and climate change intensifies, there is a growing  
18 demand for local scale monitoring of current and future climate change. Assessing and planning  
19 the adaptation to the expected unprecedented impacts of climate change on humans activities,  
20 ecosystems and the biosphere as a whole, require an accurate local information with well calibrated  
21 uncertainties. This need relates to estimates of warming to date and the future warming in response  
22 to set of scenarios of future greenhouse gas emissions.

23 There is now clear evidence that the recent increase of the average Earth's temperature is mostly  
24 due to human activities (Bindoff et al. 2013; Lee et al. 2021). Concurrently, the anthropogenic  
25 influence is not detected everywhere at the local scale (Hawkins and Sutton 2012; Hawkins et al.  
26 2020). Natural climate variability can blur the emergence of the anthropogenic signal for the next  
27 few years at high latitudes, while a significant warming is already reported in several tropical regions  
28 (Deser et al. 2012; Mahlstein et al. 2011). Regarding climate projections, the IPCC concluded  
29 in its 5th assessment report (AR5) (Collins et al. 2013), that "Future [human-induced] warming  
30 trends cannot be predicted precisely, especially at local scales".

31 In the IPCC AR6 (Lee et al. 2021), a new generation of climate models (Eyring et al. 2016)  
32 has been used to provide a range of projections in response to different socio-economic scenarios  
33 (O'Neill et al. 2016). Based on this new dataset, various studies have recently shown that uncertainty  
34 in global mean warming can be considerably reduced by using the information provided by recent  
35 observed warming trends via so-called "constraint" methods (Tokarska et al. 2020; Ribes et al.  
36 2021; Brunner et al. 2020a; Nijssen et al. 2020). These studies consistently point towards a downward  
37 revision of the expected warming in all emission scenarios (Brunner et al. 2020a; Tokarska et al.  
38 2020), with a decrease in model uncertainty of nearly 40% for end of century projections (Ribes  
39 et al. 2021), and even more at shorter lead times. This is an important result as, until then,  
40 observations have failed to provide clear evidence in reducing the range of climate projections  
41 (Schlund et al. 2020).

42 The next challenge is to transpose these new findings on global warming to regional and local  
43 scales. At the regional scale, a few studies have adopted the partitioning from the Special Report  
44 on Managing the Risks of Extreme Events and Disasters to Advance Climate Change Adaptation  
45 (Field et al. 2012) (SREX) and have attempted to narrow model uncertainty with sophisticated

46 techniques with promising results (Brunner et al. 2020b, 2019). But the SREX regions are  
47 typically continental-wide, and do not provide relevant information for local adaptation. At the  
48 local scale (defined as the size of a global climate model grid box of about 200 km), and to the best  
49 of our knowledge, only a few studies have attempted to narrow climate model uncertainty, by using  
50 weighting methods to account for inter-dependencies between models (Abramowitz and Bishop  
51 2015; Bishop and Abramowitz 2013), or by focusing on specific and limited areas (Borodina et al.  
52 2017). In particular, although constrained GSAT projections are now used in the AR6 (Lee et al.  
53 2021), local climate projections are still solely based on a raw ensemble of available climate models  
54 (<https://interactive-atlas.ipcc.ch/>), derived from global warming levels.

55 In this paper, we assess how much uncertainty in local temperature projections can be reduced in  
56 global climate models. Section 2 describes the methods and details the observation and model data.  
57 In section 3, first we take advantage of the tight links that exist between local climate and GMST  
58 (Sutton et al. 2015; Tebaldi and Arblaster 2014). Specifically, we describe the local implications of  
59 the recent advances in the reduction of the uncertainties in GMST projections. Then, we provide  
60 a set of local-scale temperature projections, which encapsulate another source of information:  
61 the observed local warming to date. If compared to the global mean temperature record, local  
62 observations are typically more affected by internal variability and measurement uncertainty. Yet,  
63 they still provide a useful source of information on both past and future trends, particularly over  
64 some specific regions. Then, we evaluate these results and discuss how much these two types of  
65 observations (global and local) narrow uncertainty on future warming ranges. Such a reduction is  
66 expected to provide more accurate information that becomes critical for policy-makers in the local  
67 climate risk management (Viner et al. 2020), as well as for the climate science community.

## 68 **2. Methods and data**

### 69 *a. Observational dataset and models*

70 The temperature observations are from the Cowtan and Way (2014) (hereafter CW) dataset which  
71 complements the HadCRUT4 (Morice et al. 2012) data by filling in the missing data over the 1850-  
72 2019 period. The temperature field comes from a blending of near-surface temperature and sea  
73 surface temperature using land sea mask and sea ice concentration. The measurement uncertainty  
74 of the CW dataset is estimated from a ensemble of 100 equiprobable realisations. Most of the other

75 observational products are included in the temperature range estimated by this ensemble, which  
 76 confirms our choice to consider the CW dataset as a reference.

77 Climate models are selected from the CMIP6 ensemble (Eyring et al. 2016) according to the  
 78 availability of the following data: at least 200 years of pre-industrial control simulation; at least  
 79 one member of a historical simulation and one member of a projection simulation for the SSP5-8.5  
 80 scenario. In order to constrain the simulated temperatures at a grid point scale in a consistent way,  
 81 a blended temperature field  $T_{\text{blend}}$  is computed in each CMIP6 model based on the formulation of  
 82 Cowtan et al. (2015):

$$\begin{cases} w_{\text{air}} &= (1 - f_{\text{ocean}}) + f_{\text{ocean}}f_{\text{ice}}, \\ T_{\text{blend}} &= w_{\text{air}}T_{\text{air}} + (1 - w_{\text{air}})T_{\text{ocean}}, \end{cases} \quad (1)$$

83 where  $T_{\text{air}}$ ,  $T_{\text{ocean}}$ ,  $f_{\text{ice}}$ , and  $f_{\text{ocean}}$  are for each grid point near-surface air temperature, sea surface  
 84 temperature, sea ice concentration and sea area fraction. The 27 models for which these variables  
 85 are available and which satisfy the above criteria are listed in Table 1.

86 We define the global surface air temperature (GSAT) as the global mean of  $T_{\text{air}}$  and the global  
 87 mean surface temperature (GMST) as the global mean of  $T_{\text{blend}}$ . Several studies have shown that  
 88 GMST and GSAT significantly differ as GMST warms significantly less than GSAT (Cowtan et al.  
 89 2015; Richardson et al. 2018).

90 Models are interpolated on a common horizontal grid of  $2.5^\circ$  resolution before calculating  
 91 blended temperatures and applying the constraining method. This choice is motivated by a  
 92 compromise between the different resolutions of the CMIP6 models (between  $1.5^\circ$  and  $2.5^\circ$ ).  
 93 Note that the KCC method can be applied to finer resolutions if observations are available at this  
 94 scale. For temperature, for which the spatial autocorrelation is high, the reduction in the uncertainty  
 95 is expected to be the similar as for the  $2.5^\circ$  resolution.

## 98 *b. Statistical Method*

99 The statistical method is based on the same one used by Ribes et al. (2021), whose formulation and  
 100 principle is similar to kriging, which is a method originally developed to interpolate geophysical  
 101 data based on prior covariances. In Ribes et al. (2021), this method is applied to the analysis  
 102 of time series from climate simulations of CMIP5 and CMIP6 models, and is used for several

Model	Number of members
ACCESS-CM2	1
ACCESS-ESM1-5	3
BCC-CSM2-MR	1
CanESM5-CanOE	3
CanESM5	50
CESM2	2
CESM2-WACCM	1
CNRM-CM6-1	6
CNRM-CM6-1-HR	1
CNRM-ESM2-1	5
EC-Earth3	7
EC-Earth3-Veg	3
FGOALS-g3	1
FIO-ESM-2-0	3
GFDL-ESM4	1
HadGEM3-GC31-LL	1
INM-CM4-8	1
INM-CM5-0	1
IPSL-CM6A-LR	6
MIROC6	3
MIROC-ES2L	1
MPI-ESM1-2-HR	2
MPI-ESM1-2-LR	10
MRI-ESM2-0	1
NESM3	1
NorESM2-MM	1
UKESM1-0-LL	5
27 models	121 members

96 TABLE 1. List of the available CMIP6 Models and the associated number of members in the historical and  
97 SSP5-8.5 simulations used to constrain temperature projections.

103 purposes: (i) reducing model uncertainty on past and future global warming estimated by CMIP  
104 and ScenarioMIP (O'Neill et al. 2016) simulations, (ii) reducing uncertainty on warming attributed  
105 to several external forcings via DAMIP (Gillett et al. 2016) models, (iii) complete or statistically  
106 reconstruct missing simulations from other physically relevant simulations (e.g. using the so-called  
107 1%CO<sub>2</sub> simulations, in which the CO<sub>2</sub> concentration increases by 1% each year, to reconstruct  
108 DAMIP historical simulations in which GHGs follow their historical concentrations, while other  
109 forcings are kept constant). Here we apply this method of Kriging for Climate Change (KCC)  
110 to reduce the model uncertainty in the past and future temperature changes simulated by CMIP6

111 models at each grid point. Note that a confusion can be made with techniques based on so-called  
 112 emergent constraints methods (Hall and Qu 2006; Hall et al. 2019). Emergent constraints would  
 113 usually consider the sole observed global warming trend (a single scalar); e.g. over the 1980-  
 114 2019 period, to constrain the simulated temperature changes in the future. The KCC method  
 115 has several advantages compared to this approach. Instead of simply constraining a trend over a  
 116 sub-period, it uses the entire observed time series of temperature, which avoids ignoring useful  
 117 information. In addition, the method takes into account the model temporal pattern uncertainty,  
 118 and provides confidence ranges specifically for the forced response, while many other studies also  
 119 include internal variability.

120 For a given grid point, we define  $\mathbf{y}_{\text{loc}}^*$  as the yearly time series of the real (and unknown)  
 121 temperature response to external forcings over the 1850-2019 period, and  $\mathbf{y}_{\text{loc}}$  as the observed  
 122 yearly temperature time series over the same period. Similarly, we define for the GMST the  
 123 vectors  $\mathbf{y}_{\text{glo}}^*$  and  $\mathbf{y}_{\text{glo}}$  as the unknown response to external forcings and the observed time series,  
 124 respectively. They constitute the following  $\mathbf{y}^*$  and  $\mathbf{y}$  vectors, both of size  $2n_y$  where  $n_y = 170$ :

$$\mathbf{y}^* = \begin{pmatrix} \mathbf{y}_{\text{loc}}^* \\ \mathbf{y}_{\text{glo}}^* \end{pmatrix}, \quad \mathbf{y} = \begin{pmatrix} \mathbf{y}_{\text{loc}} \\ \mathbf{y}_{\text{glo}} \end{pmatrix}. \quad (2)$$

125 Assuming that the observed temperature total variability can be decomposed as the sum of a  
 126 term of forced variability and a term including both internal variability and measurement errors,  $\mathbf{y}$   
 127 takes the following form:

$$\mathbf{y} = \mathbf{y}^* + \boldsymbol{\epsilon}, \quad (3)$$

128 where  $\boldsymbol{\epsilon} = (\boldsymbol{\epsilon}_{\text{loc}}, \boldsymbol{\epsilon}_{\text{glo}})$  is a vector of size  $2n_y$ , and corresponds to the local and global terms  
 129 of measurement errors and observed internal variability. Further assuming that models are in-  
 130 distinguishable from the truth, *i.e.*, that observations and models are exchangeable (Annan and  
 131 Hargreaves 2010; Ribes et al. 2017; Rougier et al. 2013), observations  $\mathbf{y}$  can be rewritten:

$$\begin{cases} \mathbf{x} &= \begin{pmatrix} \mathbf{x}_{\text{loc}} \\ \mathbf{x}_{\text{glo}} \end{pmatrix}, \\ \mathbf{y} &= \mathbf{H}\mathbf{x} + \boldsymbol{\epsilon}, \end{cases} \quad (4)$$

132 where  $\mathbf{x}_{\text{loc}}$  and  $\mathbf{x}_{\text{glo}}$  are the yearly time series over the 1850-2100 period of the local and global  
 133 temperature responses to external forcings estimated in CMIP6 models, respectively, i.e. vectors  
 134 of size  $n_x = 251$ .  $\mathbf{H}$  is an observation operator of size  $2n_y \times 2n_x$ , which extracts the part of  $\mathbf{x}$  that  
 135 is observed in  $\mathbf{y}$ , i.e., the forced response from 1850 to 2019, and whose form depends on the type  
 136 of the applied constraint (using only GMST observations or both GMST and local observations,  
 137 see equation A21). Note that the assumption of exchangeability between observations and models  
 138 has been suggested as well supported by observations, especially for temperature (Annan and  
 139 Hargreaves 2010; Oldenborgh et al. 2013).

140 For a given CMIP6 model  $m$  listed in Table 1, we choose to estimate the simulated response  
 141 to all external forcings  $\mathbf{x}_{m,\text{glo}}$ , by decomposing the simulated GMST over 1850-2100 into an  
 142 anthropogenic response  $\mathbf{x}_{m,\text{ant,glo}}$ , and a natural response  $\mathbf{x}_{m,\text{nat,glo}}$ . Therefore, after averaging all  
 143 available members of the model  $m$ , the simulated GMST time series over 1850-2100  $\mathbf{x}_{m,\text{glo}}$  writes:

$$\mathbf{x}_{m,\text{glo}} = \mathbf{x}_{m,\text{nat,glo}} + \mathbf{x}_{m,\text{ant,glo}} + \boldsymbol{\epsilon}_m, \quad (5)$$

144 where  $\boldsymbol{\epsilon}_m$  is a random term for internal variability.

145 To estimate  $\mathbf{x}_{m,\text{nat,glo}}$  and  $\mathbf{x}_{m,\text{ant,glo}}$  in the model  $m$ , we use a Generalized Additive Model (GAM)  
 146 to compute the response to all external forcings,  $\mathbf{x}_{m,\text{glo}}$  (recall that  $\mathbf{x}_{m,\text{glo}}$  follows equation 4):

$$\begin{cases} \mathbf{x}_{m,\text{glo}} &= \mathbf{x}_{m,\text{all,glo}} + \boldsymbol{\epsilon}_m, \\ \mathbf{x}_{m,\text{all,glo}} &= \underbrace{\beta_m \mathbf{e}}_{\mathbf{x}_{m,\text{nat,glo}}} + \underbrace{f(\mathbf{t})}_{\mathbf{x}_{m,\text{ant,glo}}}, \end{cases} \quad (6)$$

147 where  $\beta_m$  is an unknown scaling factor.  $e$  is the multimodel mean of the temperature response  
 148 from an Energy Balance Model (EBM) using the EBM parameters from Geoffroy et al. (2013),  
 149 and is a vector of size  $n_x$ .  $f(t)$  is a time series (with  $t = (1850, \dots, 2100)$ ) and refers to an  
 150 assumed smoothed response of GMST to the anthropogenic forcings. The function  $f$  corresponds  
 151 to smoothing splines to filter out most of internal variability, with 6 degrees of freedom (a value  
 152 which was selected as a bias-variance trade-off).

153 We apply the exact same procedure to estimate the local forced responses as simulated by each  
 154 CMIP6 model. For each grid point from the model  $m$ , we consider  $x_{m,loc}$ , the average of all  
 155 available members, to estimate the local forced response,  $x_{m,all,loc}$ . We assume that the local  
 156 natural response scales linearly with the globally-averaged natural forcings time series, as the EBM  
 157 response  $e$  used to calculate  $x_{m,nat,glo}$  is also used when we fit the GAM to compute the local natural  
 158 response  $x_{m,nat,loc}$ . Thus  $x_{m,nat,glo}$  and  $x_{m,nat,loc}$  only differ by their scaling factor  $\beta_m$ . We believe  
 159 that our results are not sensitive to this choice given the reduced strength of, and uncertainty in,  
 160 the natural response compared to the anthropogenic response.

161 The multimodel ensemble of the local and global simulated responses to all external forcings is  
 162 used to derive a prior distribution of  $x$ , noted  $\Pi(x) \sim \mathcal{N}(\mu, \Sigma_{mod})$ , built from all  $x_{m,glo}$  and  $x_{m,loc}$ .  
 163  $\mu = (\mu_{loc}, \mu_{glo})$  is a vector of size  $2n_x$  and is the multimodel ensemble mean of the concatenated  
 164 local and global forced responses.  $\Sigma_{mod}$  is a variance-covariance matrix of size  $2n_x \times 2n_x$  that  
 165 describes the model spread, with the following form:

$$\Sigma_{mod} = \left[ \begin{array}{c|c} \Sigma_{mod,loc} & \Sigma_{mod,dep} \\ \hline \Sigma'_{mod,dep} & \Sigma_{mod,glo} \end{array} \right], \quad (7)$$

166 where  $\Sigma_{mod,loc}$  and  $\Sigma_{mod,glo}$  are the sample covariance matrices of size  $n_x \times n_x$  modelling local  
 167 and global model spread within  $x_{loc}$  and  $x_{glo}$ , respectively.  $\Sigma_{mod,dep}$  is the covariance matrix  
 168 modelling the dependence between  $x_{loc}$  and  $x_{glo}$ .

169 In our Bayesian framework,  $\Pi(x)$  is a first (probabilistic) estimate of  $x$ , which makes no use of  
 170 observations, and is only based on climate models. We want to update this estimate by incorporating  
 171 the observational evidence provided by  $y$ . Following the Bayesian theory, the calculation of the

172 posterior distribution  $p(\mathbf{x}|\mathbf{y})$  is required. A pre-requisite is to define the observational uncertainty,  
 173 i.e., the covariance matrix associated with  $\mathbf{y}$ .

## 174 1) MODELLING OF OBSERVATIONAL UNCERTAINTY

175 Given equation 4, we assume that  $\epsilon \sim \mathcal{N}(\mathbf{0}, \boldsymbol{\Sigma}_{\text{obs}})$ , where  $\boldsymbol{\Sigma}_{\text{obs}} = \boldsymbol{\Sigma}_{\text{meas.}} + \boldsymbol{\Sigma}_{\text{iv}}$  is the observation  
 176 error covariance matrix.  $\boldsymbol{\Sigma}_{\text{meas.}}$  and  $\boldsymbol{\Sigma}_{\text{iv}}$  are both of size  $2n_y \times 2n_y$  and describe the measurement  
 177 error and internal variability, respectively.  $\boldsymbol{\Sigma}_{\text{meas.}}$  is estimated as the sample covariance matrix over  
 178 the 100-member ensemble of the CW dataset.

179  $\boldsymbol{\Sigma}_{\text{iv}}$  is estimated by using observed annual time series of global and local temperature over the  
 180 1850-2019 period. First, we compute the global observational residuals by subtracting the CMIP6  
 181 response to all external forcings  $\boldsymbol{\mu}_{\text{glo}}(1, \dots, n_y)$  to the observations  $\mathbf{y}_{\text{glo}}$ . Similarly, we derive local  
 182 residuals by subtracting  $\boldsymbol{\mu}_{\text{loc}}(1, \dots, n_y)$  to  $\mathbf{y}_{\text{loc}}$ . These residuals constitute an estimate of global  
 183 and local internal variability.

184 We define  $\boldsymbol{\Sigma}_{\text{iv}}$  as a matrix of size  $2n_y \times 2n_y$  of the following form:

$$\boldsymbol{\Sigma}_{\text{iv}} = \left[ \begin{array}{c|c} \boldsymbol{\Sigma}_{\text{iv,loc}} & \boldsymbol{\Sigma}_{\text{iv,dep}} \\ \hline \boldsymbol{\Sigma}'_{\text{iv,dep}} & \boldsymbol{\Sigma}_{\text{iv,glo}} \end{array} \right], \quad (8)$$

185 where  $\boldsymbol{\Sigma}_{\text{iv,loc}}$  and  $\boldsymbol{\Sigma}_{\text{iv,glo}}$  are the covariance matrices of size  $n_y \times n_y$  modelling local and global  
 186 internal variability within  $\mathbf{y}_{\text{loc}}$  and  $\mathbf{y}_{\text{glo}}$ , respectively.  $\boldsymbol{\Sigma}_{\text{iv,dep}}$  is the covariance matrix modelling  
 187 the dependence between global and local temperature.

188 To compute  $\boldsymbol{\Sigma}_{\text{iv}}$ , we take into account decadal internal variability that exists in the global (Parsons  
 189 et al. 2020), regional (Qasmi et al. 2017), and even local (Laepple and Huybers 2014) observations,  
 190 by using a mixture of two autoregressive processes of order 1 (AR1), hereafter MAR, as done by  
 191 Ribes et al. (2021). The MAR formulation includes a fast (f) and a slow (s) components such that  
 192 global internal variability  $\epsilon_{\text{iv,glo}}$  within the GMST residuals writes at a time  $t$ :

$$\begin{cases} \epsilon_{iv, glo}(t) &= \epsilon_{iv, f, glo}(t) + \epsilon_{iv, s, glo}(t), \\ \epsilon_{iv, f, glo}(t) &= \alpha_{f, glo} \epsilon_{iv, f, glo}(t-1) + Z_{f, glo}(t), \\ \epsilon_{iv, s, glo}(t) &= \alpha_{s, glo} \epsilon_{iv, s, glo}(t-1) + Z_{s, glo}(t), \end{cases} \quad (9)$$

193 where the parameters  $\alpha_{s, glo}$  and  $\alpha_{f, glo}$  are the lag 1 coefficients of the AR1 processes, and  
 194  $\alpha_{s, glo} \geq \alpha_{f, glo}$  by convention.  $Z_{s, glo}(t) \sim \mathcal{N}(0, \sigma_{s, glo}^2)$  and  $Z_{f, glo}(t) \sim \mathcal{N}(0, \sigma_{f, glo}^2)$  are white noises  
 195 associated with the two AR1. The slow component is able to generate a dependence on time  
 196 scales of typically one decade, while the fast component accounts for interannual variability.  
 197 Following the principle of parsimony, only 4 coefficients ( $\sigma_{f, glo}^2, \alpha_{f, glo}, \sigma_{s, glo}^2, \alpha_{s, glo}$ ) are thus needed  
 198 to characterize internal variability at the global scale. We fill the covariance matrix  $\Sigma_{iv, glo}$  following  
 199 the calculations of each of its coefficients, as detailed in equations A2-A8. In practice, we apply  
 200 a maximum likelihood procedure to the local and global residuals according to the statistical  
 201 model from equation 9. Uncertainty related to these coefficients is not taken into account. Then,  
 202 we make the same assumptions, and estimate 4 other parameters, ( $\sigma_{f, loc}^2, \alpha_{f, loc}, \sigma_{s, loc}^2, \alpha_{s, loc}$ ), to  
 203 characterize fast and slow components in local internal variability  $\epsilon_{iv, loc}$  and to compute  $\Sigma_{iv, loc}$ .  
 204 The autocorrelations from this MAR model suggest that our statistical representation of internal  
 205 variability effectively captures decadal variability (typically between lag 5 and lag 10) in the GMST  
 206 and local temperature time series, e.g., for the Atlantic, African and South American regions (Fig.  
 207 S2). We are aware that initial condition large ensembles and long pre-industrial control (piControl)  
 208 simulations provide a nice sampling of internal variability, and could also be used to estimate this  
 209 variability. However, we choose to not directly rely on it because of the huge discrepancies between  
 210 models in terms of their simulated internal variability (Parsons et al. 2020). Figs. S17 to S27  
 211 illustrate this aspect with the piControl simulations from the CMIP6 models, including those used  
 212 to build large ensembles. In all cases, the models do not converge to a consistent estimate of internal  
 213 variability. For instance, over the Atlantic ocean, many models exhibit clear pseudo-periodic low  
 214 frequency variability, while other models do not simulate decadal variability.

## 2) MODELLING OF THE DEPENDENCE BETWEEN LOCAL AND GLOBAL INTERNAL VARIABILITY

As impacts from Pacific and Atlantic decadal variability (and potential other modes of variability) on GMST have been reported over the historical period (Trenberth and Fasullo 2013; Douville et al. 2015), we need to allow a potential dependence between global and local internal variability in  $\Sigma_{iv,dep}$ . Therefore, finding a simple and parsimonious dependence model that is compatible with the MAR structure is required. Allowing the covariances  $\text{Cov}[\epsilon_{s,glo}(t), \epsilon_{s,loc}(t)]$  and  $\text{Cov}[\epsilon_{f,glo}(t), \epsilon_{f,loc}(t)]$  to be non zero is not trivial, and these terms need to be quantified to fill the covariance matrix  $\Sigma_{iv,dep}$ . Note that the fast and slow components remain always independent, and that  $\Sigma_{iv}$  is computed for each location separately, as the spatial dependence among various locations is not considered in the method. To compute  $\Sigma_{iv,dep}$ , we introduce a ninth parameter  $\lambda$  accounting for some correlation between the local vs global components in the MAR modelling. The formulation of the covariances is slightly different in this case, and the calculations are detailed in the appendix.

## 3) CALCULATION OF $p(\mathbf{x}|\mathbf{y})$

As  $\Pi(\mathbf{x})$  and  $\epsilon$  are assumed to follow normal distributions, the Gaussian conditioning theorem is applicable to derive the posterior, or the “constrained” distribution  $p(\mathbf{x}|\mathbf{y})$ . Its formulation detailed in equation A23 indicates that the method is conservative: the uncertainty in  $p(\mathbf{x}|\mathbf{y})$  is never larger than that in  $\Pi(\mathbf{x})$ . Therefore, if observed internal variability is very large, then the model uncertainty in  $p(\mathbf{x}|\mathbf{y})$  will remain very close to that in  $\Pi(\mathbf{x})$ .

### *c. Perfect model evaluation*

We evaluate the performance of the KCC method within a perfect model framework, following a leave-one-out cross-validation:

1. For a given model, we consider a single member as pseudo-observations  $\mathbf{y}$  over the 1850–2019 period (the historical simulation is extended by the SSP5-8.5 simulation over the 2015-2019 period).
2. We use the other 26 models to derive the prior  $\Pi(\mathbf{x}) \sim \mathcal{N}(\boldsymbol{\mu}, \Sigma_{mod})$ .

- 241 3. As there is no measurement uncertainty in models,  $\Sigma_{\text{meas.}}$  is null, therefore  $\Sigma_{\text{obs}} = \Sigma_{\text{iv}}$ . As done  
 242 with the real observations, internal variability within the pseudo-observations is estimated  
 243 from the difference between the pseudo-observations time series and the forced temperature  
 244 response estimated by the ensemble mean of the 26 other models.  $\Sigma_{\text{iv}}$  is then derived from  
 245 the MAR fitted on the obtained residuals.
- 246 4. We apply the KCC method using the inputs  $\mathbf{y}$ ,  $\Sigma_{\text{obs}}$ ,  $\boldsymbol{\mu}$ ,  $\Sigma_{\text{mod}}$  to calculate projected changes  
 247 constrained by pseudo-observations.
- 248 5. These 4 steps are repeated for each available member of the considered model, and for all  
 249 available models.

250 *d. Continuous Ranked Probability Score*

251 We use the continuous ranked probability score (Gneiting et al. 2005) (CRPS) to quantify the  
 252 performance of the KCC method. It is defined as the quadratic measure of discrepancy between (i)  
 253  $\mathbb{H}(x \geq y_{\text{pobs}})$ , the empirical cumulative distribution function (CDF) of a scalar pseudo-observation  
 254  $y_{\text{pobs}}$  simulated by one model and averaged over the 2081-2100 period, and (ii) the projected CDF  
 255  $G_{\text{cons}}$  of  $p(\mathbf{x}|\mathbf{y})$  (derived from all of the other models) over the same period:

$$\text{CRPS}_{\text{cons}}(G_{\text{cons}}, y_{\text{pobs}}) = \int_{\mathbb{R}} [G_{\text{cons}}(x) - \mathbb{H}(x \geq y_{\text{pobs}})]^2 dx, \quad (10)$$

256 where  $\mathbb{H}$  is the Heaviside function (note that  $x$  is here a bound variable in the integral, different  
 257 from the vector  $\mathbf{x}$  in equation 4). Similarly, we define a reference CRPS,  $\text{CRPS}_{\text{ref}}$  based on  $G_{\text{ref}}$ , the  
 258 CDF of  $\Pi(\mathbf{x})$ , the unconstrained distribution, and  $y_{\text{pobs}}$ . We can compute the continuous ranked  
 259 probability skill score (CRPSS), which quantifies the performance of the KCC method if compared  
 260 to the reference:

$$\text{CRPSS} = 1 - \frac{\text{CRPS}_{\text{cons}}}{\text{CRPS}_{\text{ref}}} \quad (11)$$

261 The CRPSS is computed over all available pseudo-observations (121 values, see Table 1).  
 262  $\text{CRPS}_{\text{cons}}$  is calculated in both GMST-only and Local+GMST cases. Therefore, the quantity

$$1 - \frac{\text{CRPS}_{\text{cons}}(\text{Local} + \text{GMST})}{\text{CRPS}_{\text{cons}}(\text{GMST} - \text{only})}$$

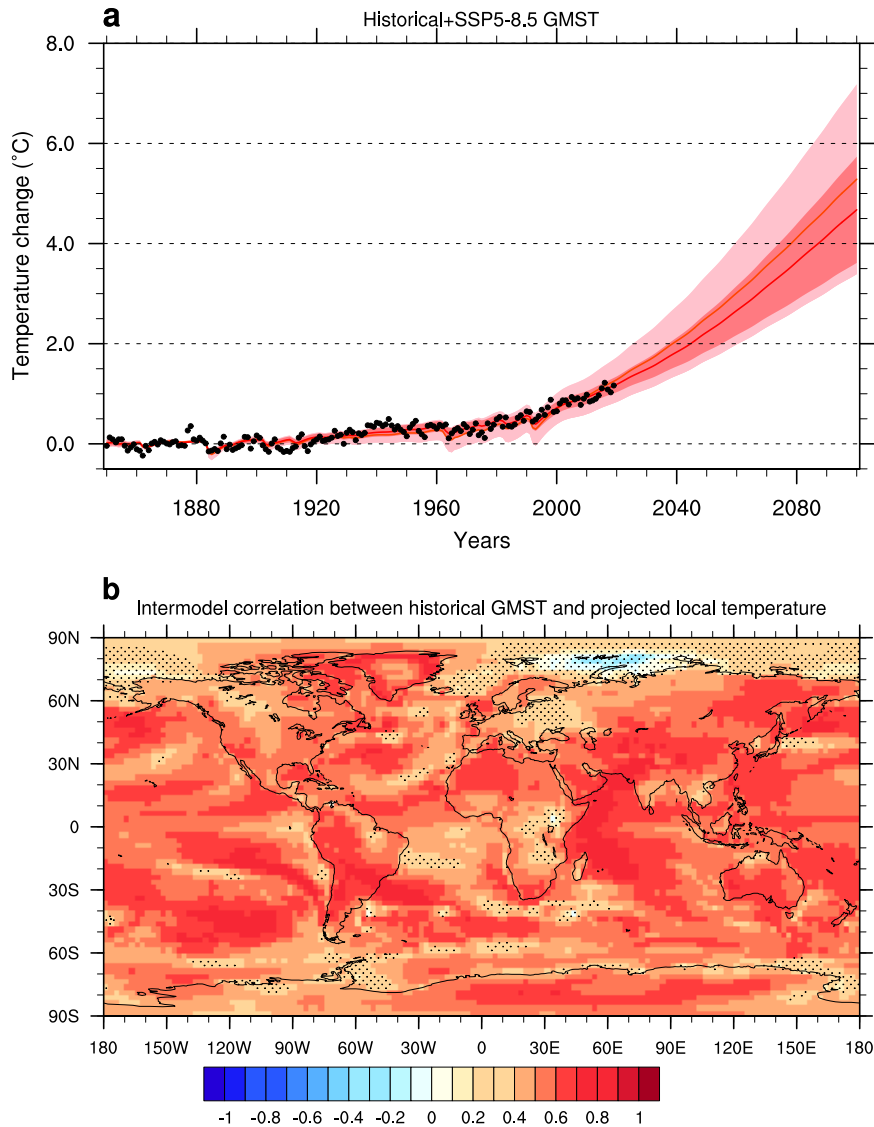
263 allows to quantify the added value from local observations compared to the sole use of GMST  
264 observations. A positive (negative) value, indicates an improvement (deterioration). The higher  
265 the CRPSS (bounded at 1), the better the performance.

### 266 **3. Results**

267 The Kriging for Climate Change (KCC) method used by Ribes et al. (2021), is one of the statistical  
268 techniques that have led to a significant reduction of uncertainty in probabilistic projections of  
269 GMST by combining observations and models. This Bayesian method involves first of all the  
270 definition of a prior distribution, which is here based on the temperature response simulated by the  
271 climate models, after filtering out internal variability as much as possible. This prior is subsequently  
272 conditioned by temperature observations over the historical period to derive a posterior probability  
273 distribution of the forced response, *i.e.*, a constrained temperature response, for both past and  
274 future periods. When applied to the GSAT time series simulated by the models from the Coupled  
275 Models Intercomparison Project phase 6 (CMIP6) (Eyring et al. 2016) models and the Shared  
276 Socio-Economic Pathway (SSP) 5-8.5 scenario, the amplitude of the projected GSAT changes  
277 constrained by the observations is revised downwards by 0.5 °C by 2100, with a reduction in model  
278 uncertainty of nearly 40% (Ribes et al. 2021). Fig. 1a offers an update of this result using GMST  
279 instead of GSAT (see Section 2 for the difference between GSAT and GMST): the warming of 5.3  
280 °C projected by CMIP6 is in this case revised downward by 0.6 °C. Differences with Ribes et al.  
281 (2021) are explained by the addition of several CMIP6 models, which affects the prior, and by  
282 the lower warming observed in GMST compared to GSAT (Cowtan et al. 2015; Richardson et al.  
283 2018). In the following, we consider the GMST metric to be consistent with the local observation  
284 dataset used (see Section 2). In this paper, we further extend this technique in order to account for  
285 multiple time series, and potential dependencies between them (see Section 2).

#### 293 *a. Constrain local climate projections with global observations*

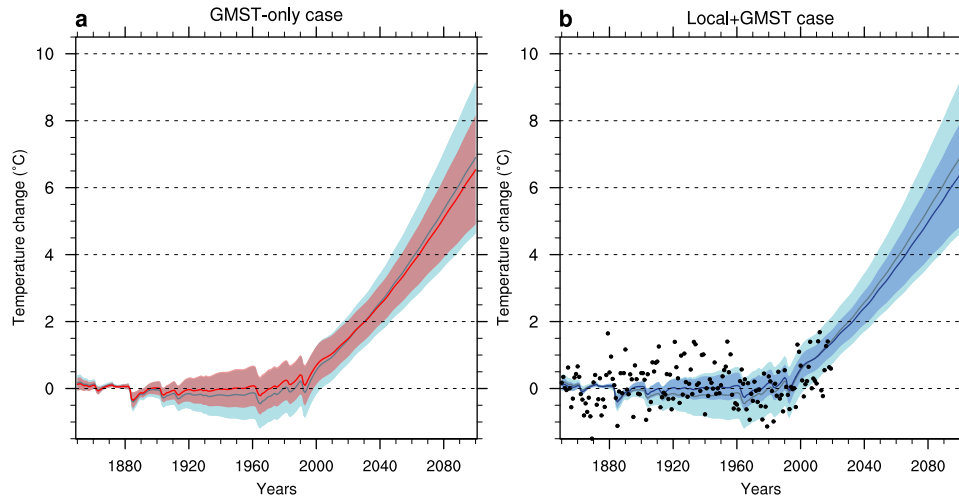
294 Climate models exhibit a strong correlation between current GMST changes and future local  
295 warming over most regions of the globe (Fig. 1b). To take such a relationship into account,  
296 we extend the KCC method to constrain local temperature projections. This is done by deriving  
297 the local warming conditional on the observed GMST record (hereafter the GMST-only case,



286 FIG. 1. (a) GMST annual observations from the Cowtan and Way (Cowtan and Way 2014) dataset (black points)  
 287 are used to constrain concatenated historical and SSP5-8.5 scenario simulations of GMST. The unconstrained  
 288 (pink) and constrained (red) ranges stand for the 5–95% confidence interval of the forced response as estimated  
 289 from 27 CMIP6 models. The thick pink (red) line stands for the ensemble mean (best estimate). All values are  
 290 anomalies with respect to the 1850–1900 period. (b) Intermodel correlation between simulated GMST trends  
 291 over the 1850-2019 period and local temperature trends over the 2020-2100 period. Stippling indicates regions  
 292 with non-significant correlation ( $p$ -value  $> 0.05$  based on a two-sided Student’s  $t$ -test).

298 see Section 2). As an example, we consider the North American city of Dallas for which the  
 299 simulated local temperature over the 2020-2100 period is significantly correlated with GMST (see

## Historical + SSP5-8.5 temperature in Dallas

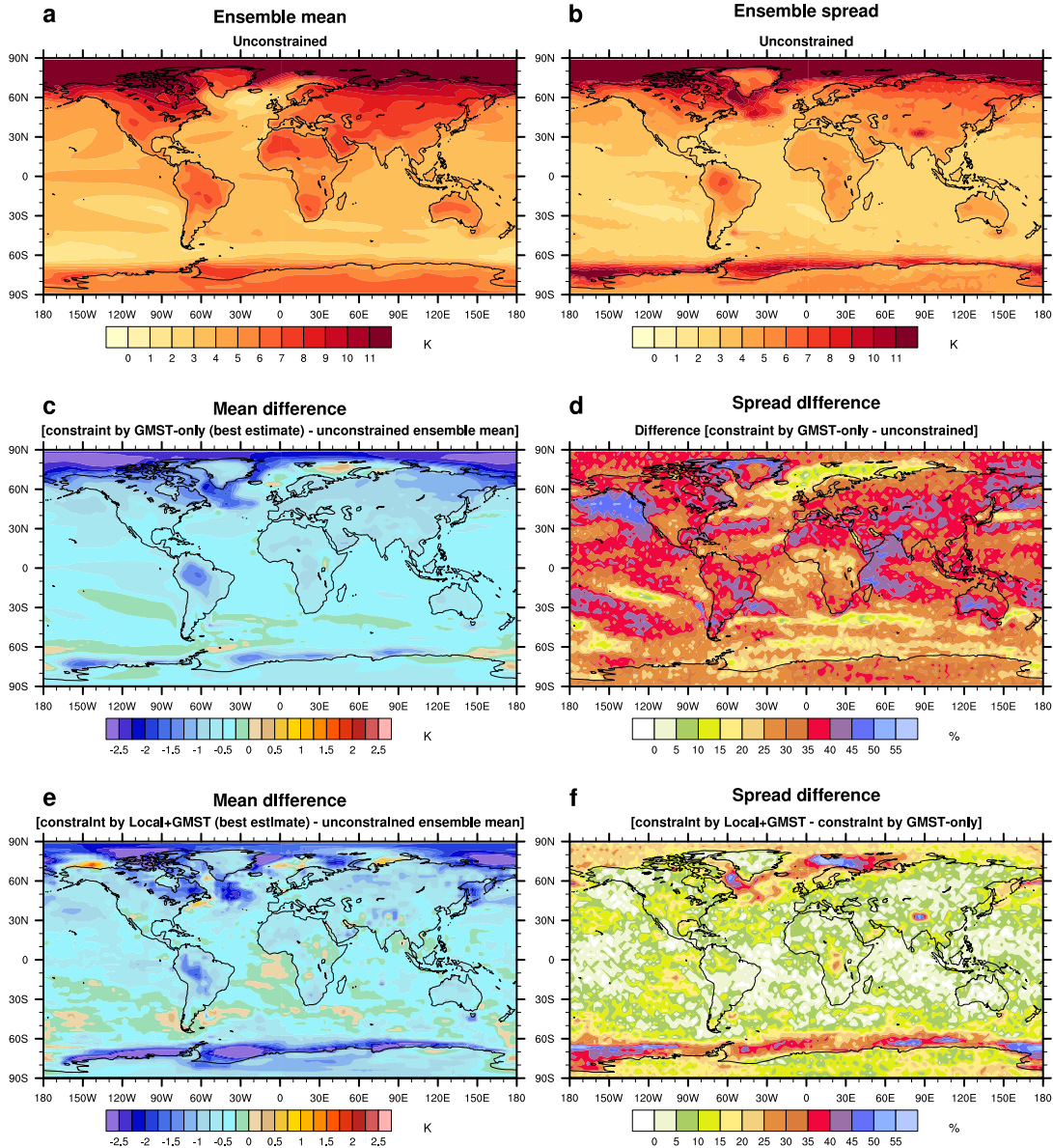


304 FIG. 2. (a) Constrained local temperature in Dallas (grid point at [48.75 °N ; 11.25 °E], see blue point 7 in  
 305 Fig. S1) in the GMST-only case. The constrained (unconstrained) 5–95% spread of the simulated response  
 306 to all external forcings is in red (light blue), the red (grey) line stands for the best estimate (ensemble mean).  
 307 (b) Constrained local temperature in the Local+GMST case. The constrained (unconstrained) 5–95% spread of  
 308 the simulated forced response is in blue (light blue), its best estimate (ensemble mean) is in dark blue (grey).  
 309 Black points are the observations. Note that because single year observations are affected by internal variability,  
 310 they often lie outside the 5–95% assessed ranges of the forced responses. Unconstrained simulated ranges are  
 311 identical between panel a) and b). All values are anomalies with respect to the 1850–1900 period.

300 the corresponding blue point 7 in Fig. S1). Consistent with the constrained GMST, the constrained  
 301 local temperature range indicates a decrease in uncertainty of about 30% over the 2081-2100 period  
 302 (Fig. 2a), and a downward revision of the best estimate of local warming by 0.4 °C compared to  
 303 the unconstrained projections (hereafter the unconstrained case).

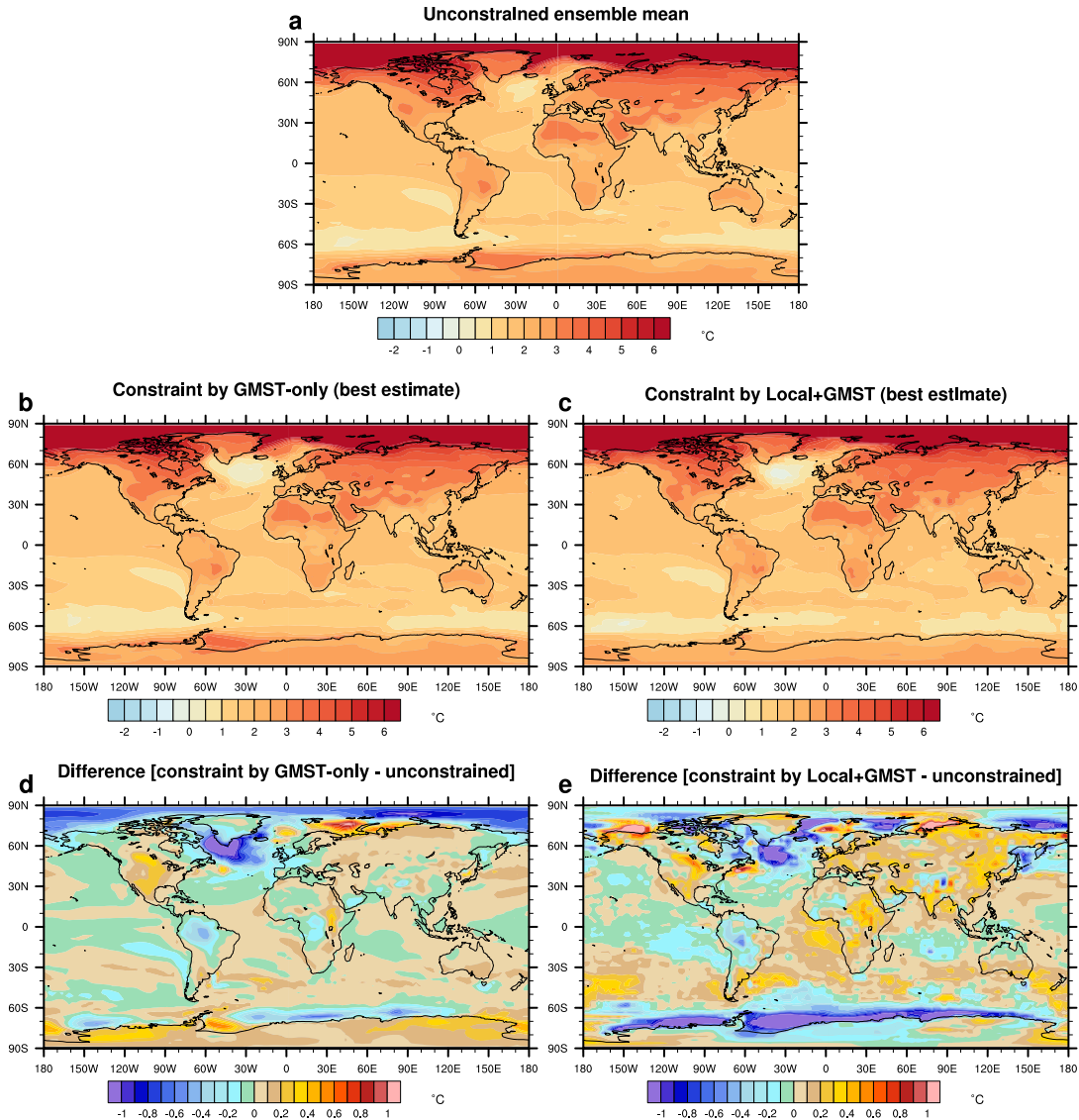
312 When the method is applied to any location worldwide, the results in the projected mean tem-  
 313 perature and in model uncertainty depend on the level of correlation between the local temperature  
 314 and GMST (Fig. 3bd and 1b). The reduction of uncertainty in local projections is the highest at the  
 315 locations where the correlation with GMST is the strongest. For these locations, e.g. over several  
 316 continental regions, the North Pacific and the Indian Ocean, a reduction of the ensemble spread of  
 317 about 40% is obtained over the 2081-2100 period. In addition, the best estimate warming is revised  
 318 downward between 0.5 °C to 1.5 °C (Fig. 3ac). Conversely, for locations where the correlation

319 is low, like in tropical Africa, the Barents Sea and the South Pacific gyre, the local temperature  
320 response is weakly constrained, with a reduction of the model uncertainty of 10% and a revision  
321 of the best estimate by 0.5 °C or less. These revised ranges lead to a warming pattern, at +2 °C of  
322 global warming, considerably different from the projections of the IPCC in its Special Report on  
323 Global Warming of 1.5 °C (Hoegh-Guldberg et al. 2018) (SR1.5) (Fig. 4abd). For example, local  
324 temperatures over North America are expected to be 0.5 °C warmer than in the unconstrained case  
325 under a global warming of 2 °C.



326 FIG. 3. (a) Ensemble mean of the unconstrained local temperature changes. (b) Ensemble spread of the  
 327 unconstrained local temperature changes, defined as the 5-95% confidence interval of the multimodel ensemble.  
 328 (c) Difference of local temperature changes ensemble mean between the GMST-only case and the unconstrained  
 329 case. (d) Relative difference of local temperature changes ensemble spread between the GMST-only case and the  
 330 unconstrained case. (e) Same as (c) but for the Local+GMST case. (f) Relative difference of local temperature  
 331 changes ensemble spread between the Local+GMST case and the GMST-only case, illustrating how much  
 332 incorporating local observations narrows uncertainty. All values are anomalies over the 2081–2100 period with  
 333 respect to the 1850–1900 period.

Mean temperature change at a +2°C GMST warming



334 FIG. 4. (a) Ensemble mean of the unconstrained local temperature changes at +2 °C of GMST warming. (b)  
 335 Best estimate of the constrained local temperature changes in the GMST-only case at +2 °C of GMST warming.  
 336 (c) Same as (b) but for the Local+GMST case. (d) Difference of local temperature changes between the GMST-  
 337 only case (best estimate) and the unconstrained case (ensemble mean). (e) Difference of local temperature  
 338 changes between the Local+GMST case (best estimate) and the unconstrained case (ensemble mean). All values  
 339 in (a), (b) and (c) are anomalies with respect to the 1850-1900 period.

340 *b. Added-value of local observations to the constraints*

341 Beyond the useful information provided by the historical GMST time-series, one further very  
342 natural question involves the consistency between the expected local response (regardless whether  
343 observed GMST is accounted for) and local historical observations. Current and past warming is  
344 spatially heterogeneous, and some regions like the Arctic are warming faster than others (Screen  
345 and Simmonds 2010) (Fig. 4a). Evidence suggests that climate models have underestimated the  
346 Arctic temperature increase over the last few years (Jansen et al. 2020). This is in contradiction  
347 with the downward revision of the Beaufort Sea temperature change that is implied by the GMST-  
348 only constraint (Fig. 3c). Therefore, it is very attractive to account for both GMST and local  
349 observations to provide local projections consistent with all available observations. Using recent  
350 local observations could particularly affect short term projections (typically over the 2020-2030  
351 period) and could provide a different picture of the constrained temperature ranges.

352 In order to make such a calculation, we derive a posterior of the expected local warming given  
353 local historical observations in addition to the GMST observations (hereafter the Local+GMST  
354 case, see Section 2 and equation A23). Following the example of Dallas considered in Fig. 2a, the  
355 constrained local temperature ranges become more consistent with local observations, particularly  
356 over the 2000-2019 period (Fig. 2b). Compared to the GMST-only case, the added value of local  
357 observations in the reduction of model uncertainty is limited in this example, with a decrease of  
358 about 10% of the confidence range width compared to the GMST-only case. Two reasons contribute  
359 to this limited impact, and must be considered for any location. First, the local signal-to-noise  
360 ratio can be small. This may happen if local internal variability or measurement uncertainty is  
361 large (i.e., local observations provide little insight on the externally-forced response). Second, the  
362 global and local responses can be highly correlated with each other, so that they partly provide the  
363 same information, leading to a limited impact of local observations on uncertainty ranges. In both  
364 cases, the model uncertainty will be only marginally reduced by local historical data.

365 The application of the Local+GMST constraint to all grid points worldwide results in a global  
366 mean projected warming which is about the same as the GMST-only case (Fig. 3ce), but with  
367 regional differences. On the one hand, for several regions over the Arctic, especially the Beaufort  
368 and Barents Seas, the warming is revised upwards compared to the unconstrained case, making the  
369 projections more consistent with recent observations, and implying a much higher warming than

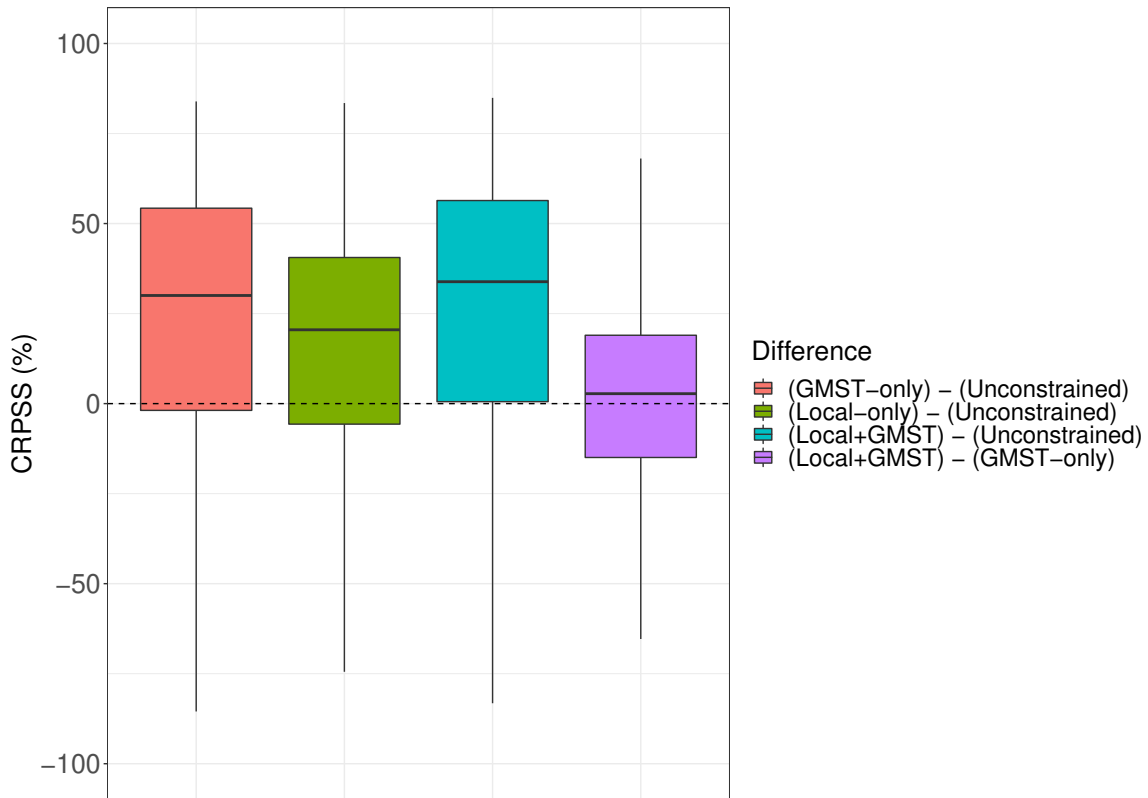
370 predicted in the GMST-only case. On the other hand, a downward revision is slightly strengthened  
371 over Northern Central Asia, Eastern North America, the East Siberian Sea, and along the Antarctica  
372 coast. The added value of local observations in the reduction of model uncertainty is the largest over  
373 these regions where the correlation in Fig. 1 is low (Fig. 3f). Note that for both the GMST-only  
374 and the Local+GMST cases, the global mean of the constrained local ranges is very close to the  
375 constrained GMST ranges shown in Fig. 1a (not shown). The addition of local information can also  
376 clearly modify the warming pattern at +2 °C of global warming (Fig. 4ce). For example, while a  
377 downward revision of the temperature change of -0.2 °C is obtained over Europe in the GMST-only  
378 case, an upward revision of 0.3 °C is obtained in the Local+GMST case. This change of sign is  
379 widespread over Eurasia. In the context of an urgent need of adaptation to the threat of climate  
380 change, our constrained warming pattern provides a revised and a more relevant information for  
381 local adaptation planning.

### 382 *c. Evaluation of the constrained projections*

383 The robustness of these promising results is quantified within a so-called perfect model frame-  
384 work, using a leave-one-out cross validation (see Section 2). Each member of each model is  
385 considered as pseudo-observations over the 1850-2019 period. These are subsequently used to  
386 constrain the temperature projections, using all other models as a prior distribution. The con-  
387 strained temperature range is then compared to the warming simulated by the model from which  
388 pseudo-observations were taken. As making this evaluation for all the grid points is computa-  
389 tionally expensive, this procedure is applied to 55 locations, considered as representative of the  
390 diversity of the worldwide climate (see Fig. S1). As for the real observations, we assess both the  
391 GMST-only and Local+GMST constraints. The continuous ranked probability skill score (CRPSS)  
392 (Gneiting et al. 2005) is used to measure the accuracy of the method, taking the unconstrained  
393 projections as a baseline as a first step (see Section 2).

394 Fig. 5 shows that the median of the CRPSS distribution based on all pseudo-observations and  
395 locations is positive in the GMST-only case with an improvement of about 30% over the 2081-2100  
396 period. Depending on the location, the skill is remarkably improved by 10% to 40%, except for one  
397 location (out of 55) where it comes close to 0 (Figs. S5 to S9). In the Local+GMST case, the skill  
398 is also always positive, and lies between 10% and 50 % relative to the unconstrained case. These

399 results clearly demonstrate the performance of the method. Moreover, the comparison between  
400 the Local+GMST and the GMST-only constraints indicates that the skill is slightly improved when  
401 adding local observations to constrain projections. Over the 55 tested locations, the CRPSS is  
402 positive for 35 locations, and is slightly negative for the remaining points. The significance of this  
403 result is assessed with a binomial test. Under the null hypothesis that adding local observations  
404 has no impact on the skill (i.e. that the GMST-only and Local+GMST cases are categories equally  
405 likely, such as a coin toss), the probability of getting this result by pure chance is 2.9%. This  
406 suggests that there is a slight but significant added value in considering the constrained ranges  
407 derived from the Local+GMST case relative to the GMST-only case. A third case for which we  
408 only use local observations (Local-only case) to constrain projections indicates lower scores than  
409 in the GMST-only and Local+GMST cases (Fig. 5), and confirms that using the combination of  
410 global and local observations enhances the accuracy of the method.



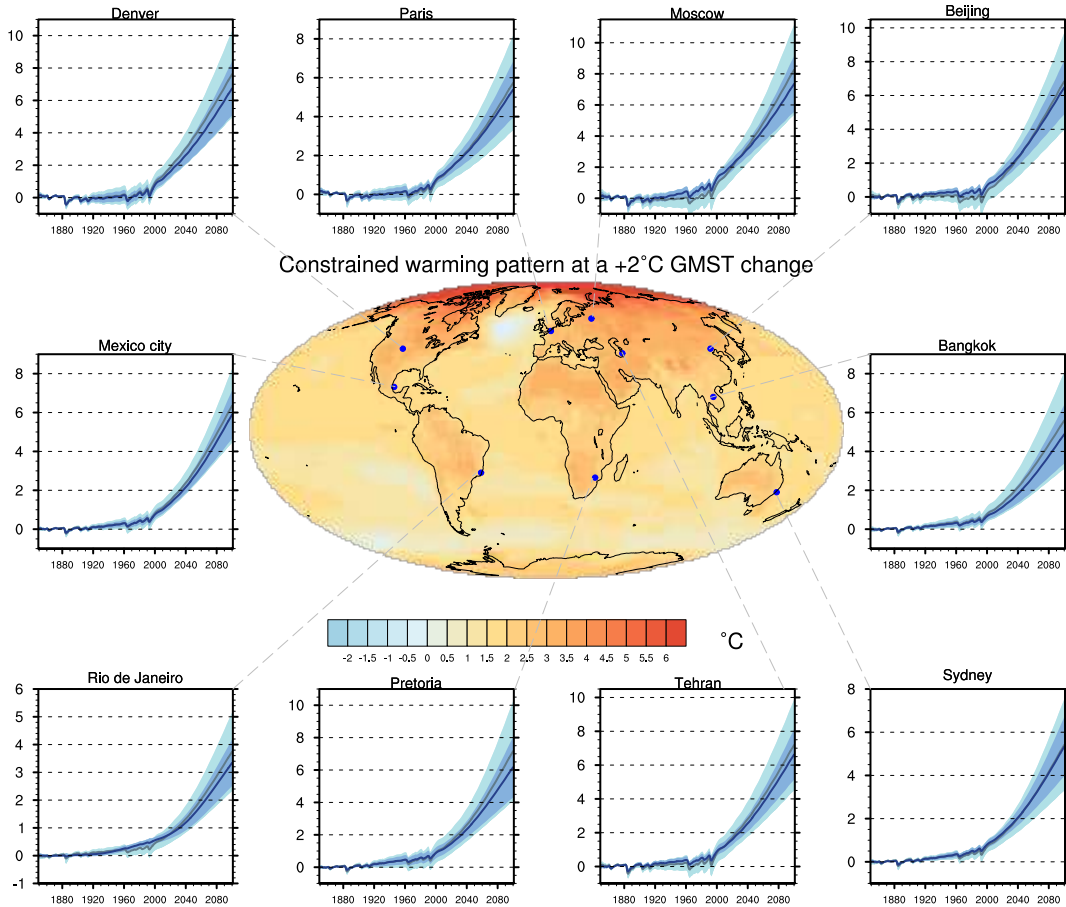
411 FIG. 5. CRPSS for the constrained temperature projections for the GMST-only, Local-only and Local+GMST  
 412 cases in red, green and blue, respectively. Calculation for each boxplot is made for all locations (see blue points  
 413 in Fig. S1) and models, over the 2081-2100 period. The boxplot in magenta indicates the added value of the  
 414 local observations and stand for the CRPSS distributions in the Local+GMST case compared to the GMST-only  
 415 case. The top (bottom) of the box represents the 25th (75th) percentile of the distribution and the upper (lower)  
 416 whisker represents the 95th (5th) percentile. Values are normalised by the number of members in each model.  
 417 A CRPSS of 0 (dashed line) indicates the absence of added value of the method.

418 Note that models with large low-frequency variability tend to pull down the CRPSS values (see  
419 Supplementary Information). A second evaluation criterion of the method based on coverage  
420 probabilities leads to similar conclusions (Supplementary Information).

421 From all of these evaluation results, we retain the Local+GMST case to provide guidance in  
422 constraining local projections. The evaluation of the KCC method suggests that the constrained  
423 temperature ranges are reliable, and demonstrate that relying on unconstrained projections to assess  
424 the local future climate is no longer the best approach.

#### 425 **4. Conclusion**

426 We have shown, using a statistical method combining the entire temperature observation records  
427 with model simulations, that uncertainty in local temperature projections can be substantially  
428 narrowed. Local projections constrained by both global and local observations exhibit a reduction  
429 of the uncertainty of 40% in average by 2100. This demonstrates the benefits of merging model  
430 simulations with observations to provide the best picture of future climate change. Fig. 6 offers  
431 a complementary perspective to the IPCC SR1.5 (Hoegh-Guldberg et al. 2018) conclusions that  
432 were solely based on raw (unconstrained) projections. For each location, a temporal evolution  
433 from 1850 to 2100 of the constrained temperature and its uncertainty can be derived, with revised  
434 projections for the near and the long term time scales. This provides a considerable revision of  
435 the local exposure to the consequences of the on-going climate change (Schleussner et al. 2016).  
436 An online tool that implements the method and illustrates the constrained temperature ranges for  
437 every point over a horizontal grid of 2.5° resolution is available via the following demonstrator:  
438 <https://saidqasmi.shinyapps.io/KCC-shinyapp/>.



439 FIG. 6. Best estimate of the constrained local temperature changes in the Local+GMST case at a +2°C GMST  
 440 warming. Similarly to Fig. 2b, the constrained and unconstrained temperature ranges are shown for several world  
 441 capitals cities over the 1850-2100 period. All values are anomalies with respect to the 1850–1900 period.

442 Promising prospects exist to improve the constrained projections. CMIP5 (Taylor et al. 2012) and  
443 CMIP6 (Eyring et al. 2016) ensembles sample model uncertainty in a probabilistic way by using  
444 all climate models as an “ensemble of opportunities” (Tebaldi and Knutti 2007; Sanderson et al.  
445 2015). This approach, in which our study fits, has several limitations that can bias the estimation  
446 of climate uncertainty (Eyring et al. 2019). One of them is that each model output is considered  
447 as independent and contributes equally to the multimodel ensemble. This “model democracy”  
448 paradigm has been largely used to summarise projection information in IPCC assessment reports  
449 (Collins et al. 2013; Lee et al. 2021), even though it can be criticised (Sanderson and Knutti 2012).  
450 Therefore, using a subset of models qualified a priori, or weighting the models in  
451 this way (Knutti et al. 2017; Sanderson et al. 2017), before applying the observational constraint,  
452 may provide even more reliable results.

453 Our results demonstrate that available observations offer valuable information to sharpen climate  
454 projections. As the climate system will continue to change over the next decades, observations will  
455 further constrain the local and the global responses to the increasing greenhouse effect. Therefore,  
456 it is critical to account for this new source of information and to regularly bridge the gap between  
457 monitoring recent changes and predicting future changes. This is particularly important as the  
458 spread among global climate models has not decreased over the last CMIP generations. With our  
459 new projection ranges, the storyline approach (Shepherd 2019; Sutton 2019; Zappa 2019), which  
460 is increasingly adopted in the climate risk management, could be refined.

461 The KCC method itself can also be improved. Although it can be used on larger areas to  
462 easily derive constrained projections, eg on the SREX regions (Brunner et al. 2020b), the current  
463 implementation does not take into account the spatial dependence in the climate variability between  
464 locations. Taking the spatial dimension fully into account could bring additional useful information  
465 and would result in consistent uncertainties at all spatial scales. In addition, generalising the method  
466 to other variables of high societal impacts, e.g. extreme precipitation, droughts, snow cover, some  
467 of which are also tightly related to GMST changes, would also be very relevant. In this way the  
468 climate science community could take a step forward towards a more accurate assessment of past  
469 and future human-induced climate change.

470 *Acknowledgments.* This work was supported by the European Union’s Horizon 2020 Research  
 471 and Innovation Programme in the framework of the EUCP project (Grant Agreement 776613) and  
 472 Météo-France. The authors thank Hervé Douville for fruitful discussions about this work. The  
 473 authors thank the climate modeling groups involved in CMIP6 exercises for producing and making  
 474 available their simulations. The authors thank Kevin Cowtan for providing the blended temperature  
 475 data, and the ETH Zurich for providing CMIP6 data through their cmip6-ng interface (<http://dx.doi.org/10.5281/zenodo.3734128>). The analyses and figures were produced with the  
 476 R software (<https://www.R-project.org/>) and the NCAR Command Language Software  
 477 (<http://dx.doi.org/10.5065/D6WD3XH5>).

479 *Data availability statement.* All required programs to run the statistical method are in the associ-  
 480 ated KCC R package, which is available under a GNU General Public License, version 3 (GPLv3),  
 481 at <https://doi.org/10.5281/zenodo.5233947> (Qasmi and Ribes 2021).

482 A reproducible example of application is provided in the Jupyter Notebook available at: [https://gitlab.com/saidqasmi/KCC\\_notebook](https://gitlab.com/saidqasmi/KCC_notebook).  
 483

## 484 APPENDIX

### 485 Complements of the statistical method

#### 486 a. Estimation of the covariance matrix $\Sigma_{iv}$

487 Recall that we define  $\Sigma_{iv}$  as a matrix of size  $2n_y \times 2n_y$  of the following form:

$$\Sigma_{iv} = \left[ \begin{array}{c|c} \Sigma_{iv,loc} & \Sigma_{iv,dep} \\ \hline \Sigma'_{iv,dep} & \Sigma_{iv,glo} \end{array} \right], \quad (A1)$$

488 where  $\Sigma_{iv,loc}$  and  $\Sigma_{iv,glo}$  are the covariance matrices of size  $n_y \times n_y$  modeling local and global  
 489 internal variability within  $\mathbf{y}_{loc}$  and  $\mathbf{y}_{glo}$ , respectively.  $\Sigma_{iv,dep}$  is the covariance matrix modeling the  
 490 dependence between the two residuals.

#### 491 1) ESTIMATION OF $\Sigma_{iv,loc}$ AND $\Sigma_{iv,glo}$

492 First, following equation 9, we decompose  $\epsilon_{iv,f,glo}(t)$  as an infinite sum using back substitutions:

$$\begin{aligned}
\epsilon_{iv,f,glo}(t) &= \alpha_{f,glo}\epsilon_{iv,f,glo}(t-1) + Z_{f,glo}(t), \\
&= \alpha_{f,glo}[\alpha_{f,glo}\epsilon_{iv,f,glo}(t-2) + Z_{f,glo}(t-1)] + Z_{f,glo}(t), \\
&= \alpha_{f,glo}^2\epsilon_{iv,f,glo}(t-2) + \alpha_{f,glo}Z_{f,glo}(t-1) + Z_{f,glo}(t), \\
&= \alpha_{f,glo}^2[\alpha_{f,glo}\epsilon_{iv,f,glo}(t-3) + Z_{f,glo}(t-2)] + \alpha_{f,glo}Z_{f,glo}(t-1) + Z_{f,glo}(t), \\
&= \alpha_{f,glo}^3\epsilon_{iv,f,glo}(t-3) + \alpha_{f,glo}^2Z_{f,glo}(t-2) + \alpha_{f,glo}Z_{f,glo}(t-1) + Z_{f,glo}(t), \\
&= \vdots \\
&= \sum_{k=0}^{\infty} \alpha_{f,glo}^k Z_{f,glo}(t-k).
\end{aligned} \tag{A2}$$

493 Similarly for the slow component,  $\epsilon_{iv,s,glo}(t) = \sum_{k=0}^{\infty} \alpha_{s,glo}^k Z_{s,glo}(t-k)$ .

494 The variance of  $\epsilon_{iv,f,glo}(t)$  is therefore:

$$\begin{aligned}
\text{Var}[\epsilon_{iv,f,glo}(t)] &= \text{Var}\left[\sum_{k=0}^{\infty} \alpha_{f,glo}^k Z_{f,glo}(t-k)\right], \\
&= \sum_{k=0}^{\infty} \text{Var}[\alpha_{f,glo}^k Z_{f,glo}(t-k)], \\
&= \sum_{k=0}^{\infty} \alpha_{f,glo}^{2k} \text{Var}[Z_{f,glo}(t-k)], \\
&= \sum_{k=0}^{\infty} \alpha_{f,glo}^{2k} \sigma_{f,glo}^2, \\
&= \sigma_{f,glo}^2 \sum_{k=0}^{\infty} \alpha_{f,glo}^{2k}, \\
&= \frac{\sigma_{f,glo}^2}{1 - \alpha_{f,glo}^2}.
\end{aligned} \tag{A3}$$

495 Similarly for the slow component,  $\text{Var}[\epsilon_{iv,s,glo}(t)] = \frac{\sigma_{s,glo}^2}{1 - \alpha_{s,glo}^2}$ .

496 The autocovariance function at lag  $h > 0$  of  $\epsilon_{iv,f,glo}$  is calculated as follows:

$$\begin{aligned}
\text{Cov}[\epsilon_{iv,f,\text{glo}}(t), \epsilon_{iv,f,\text{glo}}(t+h)] &= \mathbb{E}[\epsilon_{iv,f,\text{glo}}(t)\epsilon_{iv,f,\text{glo}}(t+h)] - \mathbb{E}[\epsilon_{iv,f,\text{glo}}(t)]\mathbb{E}[\epsilon_{iv,f,\text{glo}}(t+h)], \\
&= \mathbb{E}[\epsilon_{iv,f,\text{glo}}(t)\epsilon_{iv,f,\text{glo}}(t+h)], \\
&= \mathbb{E}\left[\left(\sum_{k=0}^{\infty} \alpha_{f,\text{glo}}^k Z_{f,\text{glo}}(t-k)\right)\left(\sum_{j=0}^{\infty} \alpha_{f,\text{glo}}^j Z_{f,\text{glo}}(t+h-j)\right)\right], \\
&= \sum_{k=0}^{\infty} \sum_{j=0}^{\infty} \alpha_{f,\text{glo}}^k \alpha_{f,\text{glo}}^j \underbrace{\mathbb{E}[Z_{f,\text{glo}}(t-k)Z_{f,\text{glo}}(t+h-j)]}_{=0 \vee j \neq k+h}, \\
&= \sum_{k=0}^{\infty} \alpha_{f,\text{glo}}^k \alpha_{f,\text{glo}}^{k+h} \sigma_{f,\text{glo}}^2, \\
&= \sigma_{f,\text{glo}}^2 \alpha_{f,\text{glo}}^h \sum_{k=0}^{\infty} \alpha_{f,\text{glo}}^{2k}, \\
&= \frac{\sigma_{f,\text{glo}}^2}{1 - \alpha_{f,\text{glo}}^2} \alpha_{f,\text{glo}}^h.
\end{aligned} \tag{A4}$$

497 Similarly for the slow component,  $\text{Cov}[\epsilon_{iv,s,\text{glo}}(t), \epsilon_{iv,s,\text{glo}}(t+h)] = \frac{\sigma_{s,\text{glo}}^2}{1 - \alpha_{s,\text{glo}}^2} \alpha_{s,\text{glo}}^h$ .

498 The slow and fast components within each residual are independent:

$$\begin{cases} \text{Cov}[\epsilon_{iv,f,\text{glo}}(t), \epsilon_{iv,s,\text{glo}}(t)] = 0, \\ \text{Cov}[\epsilon_{iv,f,\text{loc}}(t), \epsilon_{iv,s,\text{loc}}(t)] = 0. \end{cases} \tag{A5}$$

499 Therefore, the coefficients  $\Sigma_{iv,\text{glo},ij}$  and  $\Sigma_{iv,\text{loc},ij}$ , i.e. the covariances at lag  $|i-j|$  with  $(i, j) \in$   
500  $\llbracket 1, n_y \rrbracket^2$  are given by:

$$\begin{cases} \Sigma_{iv,\text{loc},ij} = \frac{\sigma_{f,\text{loc}}^2}{1 - \alpha_{f,\text{loc}}^2} \alpha_{f,\text{loc}}^{|i-j|} + \frac{\sigma_{s,\text{loc}}^2}{1 - \alpha_{s,\text{loc}}^2} \alpha_{s,\text{loc}}^{|i-j|}, \\ \Sigma_{iv,\text{glo},ij} = \frac{\sigma_{f,\text{glo}}^2}{1 - \alpha_{f,\text{glo}}^2} \alpha_{f,\text{glo}}^{|i-j|} + \frac{\sigma_{s,\text{glo}}^2}{1 - \alpha_{s,\text{glo}}^2} \alpha_{s,\text{glo}}^{|i-j|}. \end{cases} \tag{A6}$$

501 In a matrix form,  $\Sigma_{iv,\text{glo}}$  and  $\Sigma_{iv,\text{loc}}$  write:

$$\Sigma_{iv,loc} = \frac{\sigma_{f,loc}^2}{1 - \alpha_{f,loc}^2} \begin{bmatrix} 1 & \alpha_{f,loc} & \cdots & \alpha_{f,loc}^{n_y-1} \\ \alpha_{f,loc} & \ddots & \ddots & \\ \vdots & \ddots & \ddots & \alpha_{f,loc} \\ \alpha_{f,loc}^{n_y-1} & & \alpha_{f,loc} & 1 \end{bmatrix} + \frac{\sigma_{s,loc}^2}{1 - \alpha_{s,loc}^2} \begin{bmatrix} 1 & \alpha_{s,loc} & \cdots & \alpha_{s,loc}^{n_y-1} \\ \alpha_{s,loc} & \ddots & \ddots & \\ \vdots & \ddots & \ddots & \alpha_{s,loc} \\ \alpha_{s,loc}^{n_y-1} & & \alpha_{s,loc} & 1 \end{bmatrix}, \quad (A7)$$

$$\Sigma_{iv,glo} = \frac{\sigma_{f,glo}^2}{1 - \alpha_{f,glo}^2} \begin{bmatrix} 1 & \alpha_{f,glo} & \cdots & \alpha_{f,glo}^{n_y-1} \\ \alpha_{f,glo} & \ddots & \ddots & \\ \vdots & \ddots & \ddots & \alpha_{f,glo} \\ \alpha_{f,glo}^{n_y-1} & & \alpha_{f,glo} & 1 \end{bmatrix} + \frac{\sigma_{s,glo}^2}{1 - \alpha_{s,glo}^2} \begin{bmatrix} 1 & \alpha_{s,glo} & \cdots & \alpha_{s,glo}^{n_y-1} \\ \alpha_{s,glo} & \ddots & \ddots & \\ \vdots & \ddots & \ddots & \alpha_{s,glo} \\ \alpha_{s,glo}^{n_y-1} & & \alpha_{s,glo} & 1 \end{bmatrix}. \quad (A8)$$

502 2) ESTIMATION OF  $\Sigma_{iv,dep}$

503 To model the dependence between internal variability within the GMST and local internal vari-  
 504 ability in the covariance matrix  $\Sigma_{iv,dep}$ , we need to calculate the covariances  $\text{Cov}[\epsilon_{s,glo}(t), \epsilon_{s,loc}(t)]$   
 505 and  $\text{Cov}[\epsilon_{f,glo}(t), \epsilon_{f,loc}(t)]$ . We can write:

$$\begin{bmatrix} \epsilon_{f,glo}(t) \\ \epsilon_{f,loc}(t) \end{bmatrix} = \begin{bmatrix} \alpha_{f,glo} & 0 \\ 0 & \alpha_{f,glo} \end{bmatrix} \begin{bmatrix} \epsilon_{f,glo}(t-1) \\ \epsilon_{f,loc}(t-1) \end{bmatrix} + \begin{bmatrix} Z_{f,glo}(t) \\ Z_{f,loc}(t) \end{bmatrix}. \quad (A9)$$

506 This vector autoregressive model can also be written:

$$\epsilon_{f,t} = A\epsilon_{f,t-1} + Z_{f,t}, \quad (A10)$$

507 where  $\epsilon_{f,t}$  and  $Z_{f,t}$  are vectors and  $A$  is a matrix.

508 Computing the covariance of  $\epsilon_{f,t}$  gives:

$$\Sigma_{\epsilon} = A\Sigma_{\epsilon}A' + \Sigma_Z, \quad (A11)$$

509 where  $\Sigma_\epsilon = \text{Cov}[\epsilon_{f,t}]$  and  $\Sigma_Z = \text{Cov}[Z_{f,t}]$ . As we want to allow a relationship between the  
 510 local and global fast components, we slightly change the distribution parameters associated of the  
 511 white noises, and introduce a parameter  $\lambda$ , which links  $Z_{f,\text{loc}}(t)$  to  $Z_{f,\text{glo}}(t)$  in  $\Sigma_Z$  such as:

$$\Sigma_Z = \begin{bmatrix} \frac{\lambda^2 \sigma_{f,\text{loc}}^2}{1 - \alpha_{f,\text{loc}}^2} & \frac{\lambda \sigma_{f,\text{loc}} \sigma_{f,\text{glo}}}{\sqrt{1 - \alpha_{f,\text{loc}}^2} \sqrt{1 - \alpha_{f,\text{glo}}^2}} \\ \frac{\lambda \sigma_{f,\text{glo}} \sigma_{f,\text{loc}}}{\sqrt{1 - \alpha_{f,\text{glo}}^2} \sqrt{1 - \alpha_{f,\text{loc}}^2}} & \frac{\lambda^2 \sigma_{f,\text{glo}}^2}{1 - \alpha_{f,\text{glo}}^2} \end{bmatrix}. \quad (\text{A12})$$

512 Coefficients of  $\Sigma_\epsilon$  are given by solving equation A11:

$$\text{Vec}(\Sigma_\epsilon) = [I - A \otimes A']^{-1} \text{Vec}(\Sigma_Z), \quad (\text{A13})$$

513 where  $\text{Vec}$  stands for the vectorisation and  $\otimes$  for the Kronecker product. Equation A13 can be  
 514 written:

$$\begin{bmatrix} \text{Var}[\epsilon_{f,\text{glo}}(t)] \\ \text{Cov}[\epsilon_{f,\text{glo}}(t), \epsilon_{f,\text{loc}}(t)] \\ \text{Cov}[\epsilon_{f,\text{loc}}(t), \epsilon_{f,\text{glo}}(t)] \\ \text{Var}[\epsilon_{f,\text{loc}}(t)] \end{bmatrix} = \begin{bmatrix} 1 - \alpha_{f,\text{glo}}^2 & 0 & 0 & 0 \\ 0 & 1 - \alpha_{f,\text{glo}} \alpha_{f,\text{loc}} & 0 & 0 \\ 0 & 0 & 1 - \alpha_{f,\text{loc}} \alpha_{f,\text{glo}} & 0 \\ 0 & 0 & 0 & 1 - \alpha_{f,\text{loc}}^2 \end{bmatrix}^{-1} \begin{bmatrix} \frac{\lambda^2 \sigma_{f,\text{loc}}^2}{1 - \alpha_{f,\text{loc}}^2} \\ \frac{\lambda \sigma_{f,\text{loc}} \sigma_{f,\text{glo}}}{\sqrt{1 - \alpha_{f,\text{loc}}^2} \sqrt{1 - \alpha_{f,\text{glo}}^2}} \\ \frac{\lambda \sigma_{f,\text{glo}} \sigma_{f,\text{loc}}}{\sqrt{1 - \alpha_{f,\text{glo}}^2} \sqrt{1 - \alpha_{f,\text{loc}}^2}} \\ \frac{\lambda^2 \sigma_{f,\text{glo}}^2}{1 - \alpha_{f,\text{glo}}^2} \end{bmatrix} \quad (\text{A14})$$

515 Then we obtain:

$$\text{Cov}[\epsilon_{f,\text{glo}}(t), \epsilon_{f,\text{loc}}(t)] = \frac{\lambda \sigma_{f,\text{glo}} \sigma_{f,\text{loc}}}{\sqrt{1 - \alpha_{f,\text{glo}}^2} \sqrt{1 - \alpha_{f,\text{loc}}^2} (1 - \alpha_{f,\text{glo}} \alpha_{f,\text{loc}})}. \quad (\text{A15})$$

516 The covariance at lag  $h > 0$  between  $\epsilon_{f,\text{glo}}(t)$  and  $\epsilon_{f,\text{loc}}(t - h)$  is calculated using back substitutions:

$$\begin{aligned}
\text{Cov}[\epsilon_{f,\text{glo}}(t), \epsilon_{f,\text{loc}}(t-h)] &= \mathbb{E}[\epsilon_{f,\text{glo}}(t)\epsilon_{f,\text{loc}}(t-h)], \\
&= \mathbb{E}[\alpha_{f,\text{glo}}\epsilon_{f,\text{glo}}(t-1)\epsilon_{f,\text{loc}}(t-h)] + \underbrace{\mathbb{E}[Z_{f,\text{glo}}(t)(\epsilon_{f,\text{loc}}(t-h))]}_{=0}, \\
&= \alpha_{f,\text{glo}} \text{Cov}[\epsilon_{f,\text{glo}}(t-1), \epsilon_{f,\text{loc}}(t-h)], \\
&= \vdots \\
&= \alpha_{f,\text{glo}}^h \text{Cov}[\epsilon_{f,\text{glo}}(t-h), \epsilon_{f,\text{loc}}(t-h)], \\
&= \alpha_{f,\text{glo}}^h \frac{\lambda\sigma_{f,\text{glo}}\sigma_{f,\text{loc}}}{\sqrt{1-\alpha_{f,\text{glo}}^2}\sqrt{1-\alpha_{f,\text{loc}}^2}(1-\alpha_{f,\text{glo}}\alpha_{f,\text{loc}})}.
\end{aligned} \tag{A16}$$

517 Similarly, we can write the covariance at lag  $h > 0$  between  $\epsilon_{f,\text{glo}}(t-h)$  and  $\epsilon_{f,\text{loc}}(t)$ :

$$\text{Cov}[\epsilon_{f,\text{glo}}(t-h), \epsilon_{f,\text{loc}}(t)] = \alpha_{f,\text{loc}}^h \frac{\lambda\sigma_{f,\text{glo}}\sigma_{f,\text{loc}}}{\sqrt{1-\alpha_{f,\text{glo}}^2}\sqrt{1-\alpha_{f,\text{loc}}^2}(1-\alpha_{f,\text{glo}}\alpha_{f,\text{loc}})}. \tag{A17}$$

518 The same calculations applied to the slow components give the following covariances:

$$\begin{cases}
\text{Cov}[\epsilon_{s,\text{glo}}(t-h), \epsilon_{s,\text{loc}}(t)] &= \alpha_{s,\text{loc}}^h \frac{\lambda\sigma_{s,\text{glo}}\sigma_{s,\text{loc}}}{\sqrt{1-\alpha_{s,\text{glo}}^2}\sqrt{1-\alpha_{s,\text{loc}}^2}(1-\alpha_{s,\text{glo}}\alpha_{s,\text{loc}})}, \\
\text{Cov}[\epsilon_{s,\text{glo}}(t), \epsilon_{s,\text{loc}}(t-h)] &= \alpha_{s,\text{glo}}^h \frac{\lambda\sigma_{s,\text{glo}}\sigma_{s,\text{loc}}}{\sqrt{1-\alpha_{s,\text{glo}}^2}\sqrt{1-\alpha_{s,\text{loc}}^2}(1-\alpha_{s,\text{glo}}\alpha_{s,\text{loc}})}.
\end{cases} \tag{A18}$$

519 Therefore,  $\Sigma_{\text{iv,dep}}$  takes the form of a Toeplitz matrix:

$$\Sigma_{\text{iv,dep}} = C_f \begin{bmatrix} 1 & \alpha_{f,\text{loc}} & \cdots & \alpha_{f,\text{loc}}^{n_y-1} \\ \alpha_{f,\text{glo}} & \ddots & \ddots & \\ \vdots & \ddots & \ddots & \alpha_{f,\text{loc}} \\ \alpha_{f,\text{glo}}^{n_y-1} & & \alpha_{f,\text{glo}} & 1 \end{bmatrix} + C_s \begin{bmatrix} 1 & \alpha_{s,\text{loc}} & \cdots & \alpha_{s,\text{loc}}^{n_y-1} \\ \alpha_{s,\text{glo}} & \ddots & \ddots & \\ \vdots & \ddots & \ddots & \alpha_{s,\text{loc}} \\ \alpha_{s,\text{glo}}^{n_y-1} & & \alpha_{s,\text{glo}} & 1 \end{bmatrix}, \tag{A19}$$

520 where  $C_f = \text{Cov}[\epsilon_{f,\text{glo}}(t), \epsilon_{f,\text{loc}}(t)]$  and  $C_s = \text{Cov}[\epsilon_{s,\text{glo}}(t), \epsilon_{s,\text{loc}}(t)]$ .

521 As the correlation between local and global internal variability depends on the considered  
 522 location,  $\lambda$  is not set to a fixed value for all the grid points. Instead, for each  $\epsilon_{iv,loc}$ , we bound  $\lambda$   
 523 between -1 and 1 by considering the ratio between the empirical correlation and the correlation  
 524 associated with our MAR models. In practice,  $\lambda$  is estimated by using a method of moments:

$$\lambda = \begin{cases} -1, & \text{if } \frac{\rho_{res}}{\rho_{mar}} < -1, \\ 1, & \text{if } \frac{\rho_{res}}{\rho_{mar}} > 1, \\ \frac{\rho_{res}}{\rho_{mar}}, & \text{otherwise,} \end{cases} \quad (\text{A20})$$

525 where  $\rho_{res}$  is the correlation between the local and global observed residuals, and

$$\rho_{mar} = \frac{C_{f,max} + C_{s,max}}{\sqrt{(\sigma_{f,loc} + \sigma_{s,loc})(\sigma_{f,glo} + \sigma_{s,glo})}}$$

526 is the correlation based on the MAR parameters previously estimated from equations A7 and A8.  
 527  $C_{f,max}$  ( $C_{s,max}$ ) corresponds to the case of a total dependence between  $\epsilon_{f,glo}(t)$  and  $\epsilon_{f,loc}(t)$  ( $\epsilon_{s,glo}(t)$   
 528 and  $\epsilon_{s,loc}(t)$ ), i.e. to the covariance  $C_f$  ( $C_s$ ) with  $\lambda = 1$ .

529 The spatial pattern of  $\lambda$  is shown in Fig. S28. Overall, our statistical model remarkably captures  
 530 the dependency between local and global residuals, especially over the tropical Pacific and Atlantic  
 531 regions.

### 532 *b. Structure of the observation operator $\mathbf{H}$*

533 The observation operator  $\mathbf{H}$  is a matrix of size  $2n_y \times 2n_x$ , where  $n_y$  ( $n_x$ ) is the number of observed  
 534 (simulated) years, i.e. 170 (251) which is the length of the vectors  $\mathbf{y}_{loc}$  et  $\mathbf{y}_{glo}$  ( $\mathbf{x}_{loc}$  and  $\mathbf{x}_{glo}$ ).  
 535 When  $\mathbf{x} = (\mathbf{x}_{loc}, \mathbf{x}_{glo})$  is solely constrained by GMST observations, i.e. only by  $\mathbf{y}_{glo}$ ,  $\mathbf{H}$  extracts  
 536  $\mathbf{x}_{glo}$  from  $\mathbf{x}$  over the observed 1850-2019 period. To do so, the square submatrix  $\mathbf{H}_{glo}$  of  $\mathbf{H}$  (in  
 537 red in equation A21) is the identity matrix;  $\mathbf{H}_{loc}$  (in blue in equation A21) and all other coefficients  
 538 equal zero. Constraining by both GMST and local observations consists in setting the submatrix  
 539  $\mathbf{H}_{loc}$  and  $\mathbf{H}_{glo}$  equal to identity and all other coefficients equal to zero.

$$\mathbf{H} = \begin{array}{c} \left. \begin{array}{c} \overbrace{\left[ \begin{array}{ccc|ccc} & & & 0 & 0 & \dots & \dots & 0 \\ & & & \vdots & \vdots & & & \vdots \\ & & & 0 & 0 & \dots & \dots & 0 \\ \hline 0 & \dots & \dots & 0 & & & & 0 \\ \vdots & & & \vdots & & & & \vdots \\ 0 & \dots & \dots & 0 & & & & 0 \end{array} \right]}^{n_y} & & \overbrace{\left[ \begin{array}{ccc|ccc} & & & 0 & 0 & \dots & \dots & 0 \\ & & & \vdots & \vdots & & & \vdots \\ & & & 0 & 0 & \dots & \dots & 0 \\ \hline 0 & \dots & \dots & 0 & & & & 0 \\ \vdots & & & \vdots & & & & \vdots \\ 0 & \dots & \dots & 0 & & & & 0 \end{array} \right]}^{n_y} \\ \underbrace{\hspace{10em}}_{n_x} & & \underbrace{\hspace{10em}}_{n_y} \end{array} \right\} n_y \end{array} \quad (\text{A21})$$

540 *c. Calculation of  $p(\mathbf{x}|\mathbf{y})$*

541 Equation 4 can also be written in a matrix form:

$$\begin{bmatrix} \mathbf{x} \\ \mathbf{y} \end{bmatrix} = \begin{bmatrix} \mathbf{I} & \mathbf{0} \\ \mathbf{0} & \mathbf{H} \end{bmatrix} \begin{bmatrix} \mathbf{x} \\ \mathbf{x} \end{bmatrix} + \begin{bmatrix} \mathbf{0} \\ \boldsymbol{\epsilon} \end{bmatrix} \sim \mathcal{N} \left( \begin{bmatrix} \boldsymbol{\mu} \\ \mathbf{H}\boldsymbol{\mu} \end{bmatrix}, \begin{bmatrix} \boldsymbol{\Sigma}_{\text{mod}} & \boldsymbol{\Sigma}_{\text{mod}}\mathbf{H}' \\ \mathbf{H}\boldsymbol{\Sigma}_{\text{mod}} & \mathbf{H}\boldsymbol{\Sigma}_{\text{mod}}\mathbf{H}' + \boldsymbol{\Sigma}_{\text{obs}} \end{bmatrix} \right). \quad (\text{A22})$$

542 This formulation allows to easily derive  $\mathbf{x}|\mathbf{y}$  with the Gaussian conditioning theorem. Thus, the  
543 posterior  $p(\mathbf{x}|\mathbf{y})$  is written as follows:

$$p(\mathbf{x}|\mathbf{y} = \mathbf{y}_o) \sim \mathcal{N}(\boldsymbol{\mu} + \boldsymbol{\Sigma}_{\text{mod}}\mathbf{H}'(\mathbf{H}\boldsymbol{\Sigma}_{\text{mod}}\mathbf{H}' + \boldsymbol{\Sigma}_{\text{obs}})^{-1}(\mathbf{y}_o - \mathbf{H}\boldsymbol{\mu}), \boldsymbol{\Sigma}_{\text{mod}} - \boldsymbol{\Sigma}_{\text{mod}}\mathbf{H}'(\mathbf{H}\boldsymbol{\Sigma}_{\text{mod}}\mathbf{H}' + \boldsymbol{\Sigma}_{\text{obs}})^{-1}\mathbf{H}\boldsymbol{\Sigma}_{\text{mod}}). \quad (\text{A23})$$

## 544 **References**

- 545 Abramowitz, G., and C. H. Bishop, 2015: Climate Model Dependence and the Ensemble  
546 Dependence Transformation of CMIP Projections. *Journal of Climate*, **28 (6)**, 2332–2348,  
547 <https://doi.org/10.1175/JCLI-D-14-00364.1>, URL [https://journals.ametsoc.org/view/journals/  
548 clim/28/6/jcli-d-14-00364.1.xml](https://journals.ametsoc.org/view/journals/clim/28/6/jcli-d-14-00364.1.xml), publisher: American Meteorological Society Section: Journal  
549 of Climate.
- 550 Annan, J. D., and J. C. Hargreaves, 2010: Reliability of the CMIP3 ensem-  
551 ble. *Geophysical Research Letters*, **37 (2)**, <https://doi.org/10.1029/2009GL041994>,  
552 URL <https://agupubs.onlinelibrary.wiley.com/doi/abs/10.1029/2009GL041994>,  
553 [\\_eprint:  
https://agupubs.onlinelibrary.wiley.com/doi/pdf/10.1029/2009GL041994](https://agupubs.onlinelibrary.wiley.com/doi/pdf/10.1029/2009GL041994).
- 554 Bindoff, N. L., and Coauthors, 2013: Chapter 10 - Detection and attribution of climate change:  
555 From global to regional. *Climate Change 2013: The Physical Science Basis. IPCC Working  
556 Group I Contribution to AR5*, Cambridge University Press, Cambridge, URL [http://pure.iiasa.  
557 ac.at/id/eprint/10552/](http://pure.iiasa.ac.at/id/eprint/10552/).
- 558 Bishop, C. H., and G. Abramowitz, 2013: Climate model dependence and the replicate Earth  
559 paradigm. *Climate Dynamics*, **41 (3)**, 885–900, <https://doi.org/10.1007/s00382-012-1610-y>,  
560 URL <https://doi.org/10.1007/s00382-012-1610-y>.
- 561 Borodina, A., E. M. Fischer, and R. Knutti, 2017: Emergent Constraints in Climate Projec-  
562 tions: A Case Study of Changes in High-Latitude Temperature Variability. *Journal of Climate*,  
563 **30 (10)**, 3655–3670, <https://doi.org/10.1175/JCLI-D-16-0662.1>, URL [https://journals.ametsoc.  
564 org/view/journals/clim/30/10/jcli-d-16-0662.1.xml](https://journals.ametsoc.org/view/journals/clim/30/10/jcli-d-16-0662.1.xml), publisher: American Meteorological Soci-  
565 ety Section: Journal of Climate.
- 566 Brunner, L., R. Lorenz, M. Zumwald, and R. Knutti, 2019: Quantifying uncertainty in Eu-  
567 ropean climate projections using combined performance-independence weighting. *Environ-  
568 mental Research Letters*, **14 (12)**, 124010, <https://doi.org/10.1088/1748-9326/ab492f>, URL  
569 <https://doi.org/10.1088/1748-9326/ab492f>, publisher: IOP Publishing.
- 570 Brunner, L., A. G. Pendergrass, F. Lehner, A. L. Merrifield, R. Lorenz, and R. Knutti, 2020a: Re-  
571 duced global warming from CMIP6 projections when weighting models by performance and in-

572 dependence. *Earth System Dynamics*, **11** (4), 995–1012, [https://doi.org/https://doi.org/10.5194/](https://doi.org/https://doi.org/10.5194/esd-11-995-2020)  
573 [esd-11-995-2020](https://doi.org/https://doi.org/10.5194/esd-11-995-2020), URL <https://esd.copernicus.org/articles/11/995/2020/>, publisher: Copernicus  
574 GmbH.

575 Brunner, L., and Coauthors, 2020b: Comparing Methods to Constrain Future European Cli-  
576 mate Projections Using a Consistent Framework. *Journal of Climate*, **33** (20), 8671–8692,  
577 <https://doi.org/10.1175/JCLI-D-19-0953.1>, URL [https://journals.ametsoc.org/jcli/article/33/20/](https://journals.ametsoc.org/jcli/article/33/20/8671/348736/Comparing-Methods-to-Constrain-Future-European)  
578 [8671/348736/Comparing-Methods-to-Constrain-Future-European](https://journals.ametsoc.org/jcli/article/33/20/8671/348736/Comparing-Methods-to-Constrain-Future-European), publisher: American Mete-  
579 orological Society.

580 Collins, M., and Coauthors, 2013: Chapter 12 - Long-term climate change: Projections, com-  
581 mitments and irreversibility. *Climate Change 2013: The Physical Science Basis. IPCC Work-*  
582 *ing Group I Contribution to AR5*, IPCC, Ed., Cambridge University Press, Cambridge, URL  
583 <http://pure.iiasa.ac.at/id/eprint/10551/>.

584 Cowtan, K., and R. G. Way, 2014: Coverage bias in the HadCRUT4 tempera-  
585 ture series and its impact on recent temperature trends. *Quarterly Journal of the*  
586 *Royal Meteorological Society*, **140** (683), 1935–1944, [https://doi.org/https://doi.org/10.](https://doi.org/https://doi.org/10.1002/qj.2297)  
587 [1002/qj.2297](https://doi.org/https://doi.org/10.1002/qj.2297), URL <https://rmets.onlinelibrary.wiley.com/doi/abs/10.1002/qj.2297>,  
588 [\\_eprint: https://rmets.onlinelibrary.wiley.com/doi/pdf/10.1002/qj.2297](https://rmets.onlinelibrary.wiley.com/doi/pdf/10.1002/qj.2297).

589 Cowtan, K., and Coauthors, 2015: Robust comparison of climate models with observa-  
590 tions using blended land air and ocean sea surface temperatures. *Geophysical Research*  
591 *Letters*, **42** (15), 6526–6534, <https://doi.org/https://doi.org/10.1002/2015GL064888>,  
592 URL <https://agupubs.onlinelibrary.wiley.com/doi/abs/10.1002/2015GL064888>,  
593 [\\_eprint: https://agupubs.onlinelibrary.wiley.com/doi/pdf/10.1002/2015GL064888](https://agupubs.onlinelibrary.wiley.com/doi/pdf/10.1002/2015GL064888).

594 Deser, C., R. Knutti, S. Solomon, and A. S. Phillips, 2012: Communication of the role of  
595 natural variability in future North American climate. *Nature Climate Change*, **2** (11), 775–  
596 779, <https://doi.org/10.1038/nclimate1562>, URL <http://www.nature.com/articles/nclimate1562>,  
597 number: 11 Publisher: Nature Publishing Group.

598 Douville, H., A. Voldoire, and O. Geoffroy, 2015: The recent global warm-  
599 ing hiatus: What is the role of Pacific variability? *Geophysical Re-*  
600 *search Letters*, **42** (3), 880–888, <https://doi.org/10.1002/2014GL062775>, URL

601 <https://agupubs.onlinelibrary.wiley.com/doi/abs/10.1002/2014GL062775>, \_eprint:  
602 <https://agupubs.onlinelibrary.wiley.com/doi/pdf/10.1002/2014GL062775>.

603 Eyring, V., S. Bony, G. A. Meehl, C. A. Senior, B. Stevens, R. J. Stouffer, and K. E. Taylor, 2016:  
604 Overview of the Coupled Model Intercomparison Project Phase 6 (CMIP6) experimental design  
605 and organization. *Geoscientific Model Development*, **9** (5), 1937–1958, <https://doi.org/https://doi.org/10.5194/gmd-9-1937-2016>, URL <https://www.geosci-model-dev.net/9/1937/2016/>.

607 Eyring, V., and Coauthors, 2019: Taking climate model evaluation to the next level. *Nature Climate*  
608 *Change*, **9** (2), 102–110, <https://doi.org/10.1038/s41558-018-0355-y>, URL <https://www.nature.com/articles/s41558-018-0355-y>, number: 2 Publisher: Nature Publishing Group.

610 Field, C. B., V. Barros, and D. J. Dokken, 2012: *Managing the risks of extreme events and disasters*  
611 *to advance climate change adaption: special report of the Intergovernmental Panel on Climate*  
612 *Change*. Cambridge University Press, New York, NY, oCLC: ocn796030880.

613 Geoffroy, O., D. Saint-Martin, D. J. L. Olivié, A. Voltaire, G. Bellon, and S. Tytécá, 2013:  
614 Transient Climate Response in a Two-Layer Energy-Balance Model. Part I: Analytical So-  
615 lution and Parameter Calibration Using CMIP5 AOGCM Experiments. *Journal of Climate*,  
616 **26** (6), 1841–1857, <https://doi.org/10.1175/JCLI-D-12-00195.1>, URL <https://journals.ametsoc.org/view/journals/clim/26/6/jcli-d-12-00195.1.xml>, publisher: American Meteorological Soci-  
617 ety Section: Journal of Climate.

619 Gillett, N. P., and Coauthors, 2016: The Detection and Attribution Model Intercomparison  
620 Project (DAMIP v1.0) contribution to CMIP6. *Geoscientific Model Development*, **9** (10), 3685–  
621 3697, <https://doi.org/https://doi.org/10.5194/gmd-9-3685-2016>, URL <https://gmd.copernicus.org/articles/9/3685/2016/>, publisher: Copernicus GmbH.

623 Gneiting, T., A. E. Raftery, A. H. Westveld, and T. Goldman, 2005: Calibrated  
624 Probabilistic Forecasting Using Ensemble Model Output Statistics and Minimum  
625 CRPS Estimation. *Monthly Weather Review*, **133** (5), 1098–1118, <https://doi.org/10.1175/MWR2904.1>, URL <https://journals.ametsoc.org/mwr/article/133/5/1098/67504/Calibrated-Probabilistic-Forecasting-Using>, publisher: American Meteorological Society.

- 628 Hall, A., P. Cox, C. Huntingford, and S. Klein, 2019: Progressing emergent constraints  
629 on future climate change. *Nature Climate Change*, **9** (4), 269–278, [https://doi.org/10.1038/](https://doi.org/10.1038/s41558-019-0436-6)  
630 [s41558-019-0436-6](https://doi.org/10.1038/s41558-019-0436-6), URL <http://www.nature.com/articles/s41558-019-0436-6>.
- 631 Hall, A., and X. Qu, 2006: Using the current seasonal cycle to constrain snow albedo feed-  
632 back in future climate change. *Geophysical Research Letters*, **33** (3), [https://doi.org/10.1029/](https://doi.org/10.1029/2005GL025127)  
633 [2005GL025127](https://doi.org/10.1029/2005GL025127), URL <http://agupubs.onlinelibrary.wiley.com/doi/10.1029/2005GL025127>.
- 634 Hawkins, E., D. Frame, L. Harrington, M. Joshi, A. King, M. Rojas, and R. Sutton, 2020:  
635 Observed Emergence of the Climate Change Signal: From the Familiar to the Unknown.  
636 *Geophysical Research Letters*, **47** (6), e2019GL086259, [https://doi.org/https://doi.org/10.1029/](https://doi.org/10.1029/2019GL086259)  
637 [2019GL086259](https://doi.org/10.1029/2019GL086259), URL <http://agupubs.onlinelibrary.wiley.com/doi/abs/10.1029/2019GL086259>,  
638 [\\_eprint: https://onlinelibrary.wiley.com/doi/pdf/10.1029/2019GL086259](https://onlinelibrary.wiley.com/doi/pdf/10.1029/2019GL086259).
- 639 Hawkins, E., and R. Sutton, 2012: Time of emergence of climate signals. *Geophys-  
640 ical Research Letters*, **39** (1), [https://doi.org/https://doi.org/10.1029/2011GL050087](https://doi.org/10.1029/2011GL050087),  
641 URL <https://agupubs.onlinelibrary.wiley.com/doi/abs/10.1029/2011GL050087>, [\\_eprint:](https://agupubs.onlinelibrary.wiley.com/doi/pdf/10.1029/2011GL050087)  
642 <https://agupubs.onlinelibrary.wiley.com/doi/pdf/10.1029/2011GL050087>.
- 643 Hoegh-Guldberg, O., and Coauthors, 2018: Impacts of 1.5°C global warming on natural and human  
644 systems. *Global Warming of 1.5°C*, IPCC.
- 645 Jansen, E., and Coauthors, 2020: Past perspectives on the present era of abrupt Arctic climate  
646 change. *Nature Climate Change*, **10** (8), 714–721, <https://doi.org/10.1038/s41558-020-0860-7>,  
647 URL <http://www.nature.com/articles/s41558-020-0860-7>, number: 8 Publisher: Nature Pub-  
648 lishing Group.
- 649 Knutti, R., J. Sedláček, B. M. Sanderson, R. Lorenz, E. M. Fischer, and V. Eyring, 2017: A  
650 climate model projection weighting scheme accounting for performance and interdependence.  
651 *Geophysical Research Letters*, **44** (4), 1909–1918, <https://doi.org/10.1002/2016GL072012>,  
652 URL <https://agupubs.onlinelibrary.wiley.com/doi/abs/10.1002/2016GL072012>, [\\_eprint:](https://agupubs.onlinelibrary.wiley.com/doi/pdf/10.1002/2016GL072012)  
653 <https://agupubs.onlinelibrary.wiley.com/doi/pdf/10.1002/2016GL072012>.
- 654 Laepple, T., and P. Huybers, 2014: Ocean surface temperature variability: Large model–data  
655 differences at decadal and longer periods. *Proceedings of the National Academy of Sciences*,

656 **111 (47)**, 16 682–16 687, <https://doi.org/10.1073/pnas.1412077111>, URL [https://www.pnas.org/](https://www.pnas.org/content/111/47/16682)  
657 [content/111/47/16682](https://www.pnas.org/content/111/47/16682), publisher: National Academy of Sciences Section: Physical Sciences.

658 Lee, J., J. Marotzke, G. Bala, L. Cao, and S. Corti, 2021: Chapter 4 - Future Global Climate:  
659 Scenario-Based Projections and Near-Term Information. *Climate Change 2021: The Physical*  
660 *Science Basis. Contribution of Working Group I to the Sixth Assessment Report of the Intergov-*  
661 *ernmental Panel on Climate Change*, Cambridge University Press, Cambridge.

662 Mahlstein, I., R. Knutti, S. Solomon, and R. W. Portmann, 2011: Early onset of significant  
663 local warming in low latitude countries. *Environmental Research Letters*, **6 (3)**, 034 009,  
664 <https://doi.org/10.1088/1748-9326/6/3/034009>, URL [https://doi.org/10.1088/1748-9326/6/3/](https://doi.org/10.1088/1748-9326/6/3/034009)  
665 [034009](https://doi.org/10.1088/1748-9326/6/3/034009), publisher: IOP Publishing.

666 Morice, C. P., J. J. Kennedy, N. A. Rayner, and P. D. Jones, 2012: Quan-  
667 tifying uncertainties in global and regional temperature change using an en-  
668 semble of observational estimates: The HadCRUT4 data set. *Journal of Geo-*  
669 *physical Research: Atmospheres*, **117 (D8)**, [https://doi.org/https://doi.org/10.1029/](https://doi.org/10.1029/2011JD017187)  
670 [2011JD017187](https://doi.org/10.1029/2011JD017187), URL <https://agupubs.onlinelibrary.wiley.com/doi/abs/10.1029/2011JD017187>,  
671 [\\_eprint: https://agupubs.onlinelibrary.wiley.com/doi/pdf/10.1029/2011JD017187](https://agupubs.onlinelibrary.wiley.com/doi/pdf/10.1029/2011JD017187).

672 Nijssen, F. J. M. M., P. M. Cox, and M. S. Williamson, 2020: Emergent constraints on transient  
673 climate response (TCR) and equilibrium climate sensitivity (ECS) from historical warming in  
674 CMIP5 and CMIP6 models. *Earth System Dynamics*, **11 (3)**, 737–750, [https://doi.org/https://](https://doi.org/10.5194/esd-11-737-2020)  
675 [doi.org/10.5194/esd-11-737-2020](https://doi.org/10.5194/esd-11-737-2020), URL <https://esd.copernicus.org/articles/11/737/2020/>, pub-  
676 lisher: Copernicus GmbH.

677 Oldenborgh, G. J. v., F. J. D. Reyes, S. S. Drijfhout, and E. Hawkins, 2013: Reliability of regional  
678 climate model trends. *Environmental Research Letters*, **8 (1)**, 014 055, [https://doi.org/10.1088/](https://doi.org/10.1088/1748-9326/8/1/014055)  
679 [1748-9326/8/1/014055](https://doi.org/10.1088/1748-9326/8/1/014055), URL <https://doi.org/10.1088/1748-9326/8/1/014055>, publisher: IOP  
680 Publishing.

681 O’Neill, B. C., and Coauthors, 2016: The Scenario Model Intercomparison Project (ScenarioMIP)  
682 for CMIP6. *Geoscientific Model Development*, **9 (9)**, 3461–3482, [https://doi.org/https://doi.org/](https://doi.org/10.5194/gmd-9-3461-2016)  
683 [10.5194/gmd-9-3461-2016](https://doi.org/10.5194/gmd-9-3461-2016), URL <https://gmd.copernicus.org/articles/9/3461/2016/>, publisher:  
684 Copernicus GmbH.

- 685 Parsons, L. A., M. K. Brennan, R. C. J. Wills, and C. Proistosescu, 2020: Magnitudes and  
686 Spatial Patterns of Interdecadal Temperature Variability in CMIP6. *Geophysical Research*  
687 *Letters*, **47** (7), e2019GL086588, <https://doi.org/10.1029/2019GL086588>,  
688 URL <https://agupubs.onlinelibrary.wiley.com/doi/abs/10.1029/2019GL086588>,  
689 [\\_eprint:  
https://agupubs.onlinelibrary.wiley.com/doi/pdf/10.1029/2019GL086588](https://agupubs.onlinelibrary.wiley.com/doi/pdf/10.1029/2019GL086588).
- 690 Qasmi, S., C. Cassou, and J. Boé, 2017: Teleconnection Between Atlantic Multidecadal Vari-  
691 ability and European Temperature: Diversity and Evaluation of the Coupled Model Inter-  
692 comparison Project Phase 5 Models. *Geophysical Research Letters*, **44** (21), 11,140–11,149,  
693 <https://doi.org/10.1002/2017GL074886>, URL [https://agupubs.onlinelibrary.wiley.com/doi/abs/  
694 10.1002/2017GL074886](https://agupubs.onlinelibrary.wiley.com/doi/abs/10.1002/2017GL074886).
- 695 Qasmi, S., and A. Ribes, 2021: Kriging for Climate Change Package. URL [https://github.com/  
696 saidqasmi/KCC](https://github.com/saidqasmi/KCC), <https://doi.org/10.5281/zenodo.5233947>.
- 697 Ribes, A., S. Qasmi, and N. P. Gillett, 2021: Making climate projections conditional on historical  
698 observations. *Science Advances*, **7** (4), eabc0671, <https://doi.org/10.1126/sciadv.abc0671>, URL  
699 <https://advances.sciencemag.org/content/7/4/eabc0671>, publisher: American Association for  
700 the Advancement of Science Section: Research Article.
- 701 Ribes, A., F. W. Zwiers, J.-M. Azais, and P. Naveau, 2017: A new statistical approach to climate  
702 change detection and attribution. *Climate Dynamics*, **48** (1), 367–386, [https://doi.org/10.1007/  
703 s00382-016-3079-6](https://doi.org/10.1007/s00382-016-3079-6), URL <https://doi.org/10.1007/s00382-016-3079-6>.
- 704 Richardson, M., K. Cowtan, and R. J. Millar, 2018: Global temperature definition af-  
705 fects achievement of long-term climate goals. *Environmental Research Letters*, **13** (5),  
706 054004, <https://doi.org/10.1088/1748-9326/aab305>, URL [https://iopscience.iop.org/article/10.  
707 1088/1748-9326/aab305](https://iopscience.iop.org/article/10.1088/1748-9326/aab305).
- 708 Rougier, J., M. Goldstein, and L. House, 2013: Second-Order Exchangeability Analysis for  
709 Multimodel Ensembles. *Journal of the American Statistical Association*, **108** (503), 852–863,  
710 <https://doi.org/10.1080/01621459.2013.802963>, URL [https://doi.org/10.1080/01621459.2013.  
711 802963](https://doi.org/10.1080/01621459.2013.802963), publisher: Taylor & Francis \_eprint: <https://doi.org/10.1080/01621459.2013.802963>.

- 712 Sanderson, B. M., and R. Knutti, 2012: On the interpretation of constrained climate model  
713 ensembles. *Geophysical Research Letters*, **39** (16), <https://doi.org/10.1029/2012GL052665>,  
714 URL <https://agupubs.onlinelibrary.wiley.com/doi/abs/10.1029/2012GL052665>, \_eprint:  
715 <https://agupubs.onlinelibrary.wiley.com/doi/pdf/10.1029/2012GL052665>.
- 716 Sanderson, B. M., R. Knutti, and P. Caldwell, 2015: A Representative Democracy to Re-  
717 duce Interdependency in a Multimodel Ensemble. *Journal of Climate*, **28** (13), 5171–5194,  
718 <https://doi.org/10.1175/JCLI-D-14-00362.1>, URL [https://journals.ametsoc.org/jcli/article/28/](https://journals.ametsoc.org/jcli/article/28/13/5171/106259/A-Representative-Democracy-to-Reduce)  
719 [13/5171/106259/A-Representative-Democracy-to-Reduce](https://journals.ametsoc.org/jcli/article/28/13/5171/106259/A-Representative-Democracy-to-Reduce), publisher: American Meteorolog-  
720 ical Society.
- 721 Sanderson, B. M., M. Wehner, and R. Knutti, 2017: Skill and independence weighting for multi-  
722 model assessments. *Geoscientific Model Development*, **10** (6), 2379–2395, [https://doi.org/https://](https://doi.org/https://doi.org/10.5194/gmd-10-2379-2017)  
723 [doi.org/10.5194/gmd-10-2379-2017](https://doi.org/10.5194/gmd-10-2379-2017), URL <https://gmd.copernicus.org/articles/10/2379/2017/>,  
724 publisher: Copernicus GmbH.
- 725 Schleussner, C.-F., and Coauthors, 2016: Differential climate impacts for policy-relevant limits  
726 to global warming: the case of 1.5 °C and 2 °C. *Earth System Dynamics*, **7** (2), 327–351,  
727 <https://doi.org/10.5194/esd-7-327-2016>, URL <https://esd.copernicus.org/articles/7/327/2016/>.
- 728 Schlund, M., A. Lauer, P. Gentine, S. C. Sherwood, and V. Eyring, 2020: Emergent constraints on  
729 equilibrium climate sensitivity in CMIP5: do they hold for CMIP6? *Earth System Dynamics*,  
730 **11** (4), 1233–1258, <https://doi.org/10.5194/esd-11-1233-2020>, URL [https://esd.copernicus.org/](https://esd.copernicus.org/articles/11/1233/2020/)  
731 [articles/11/1233/2020/](https://esd.copernicus.org/articles/11/1233/2020/), publisher: Copernicus GmbH.
- 732 Screen, J. A., and I. Simmonds, 2010: The central role of diminishing sea ice in recent Arctic tem-  
733 perature amplification. *Nature*, **464** (7293), 1334–1337, <https://doi.org/10.1038/nature09051>,  
734 URL <https://www.nature.com/articles/nature09051>, number: 7293 Publisher: Nature Publish-  
735 ing Group.
- 736 Shepherd, T. G., 2019: Storyline approach to the construction of regional climate  
737 change information. *Proceedings. Mathematical, Physical, and Engineering Sciences*,  
738 **475** (2225), <https://doi.org/10.1098/rspa.2019.0013>, URL [https://www.ncbi.nlm.nih.gov/pmc/](https://www.ncbi.nlm.nih.gov/pmc/articles/PMC6545051/)  
739 [articles/PMC6545051/](https://www.ncbi.nlm.nih.gov/pmc/articles/PMC6545051/).

- 740 Sutton, R., E. Suckling, and E. Hawkins, 2015: What does global mean temperature tell us  
741 about local climate? *Philosophical Transactions of the Royal Society A: Mathematical, Physical*  
742 *and Engineering Sciences*, **373 (2054)**, 20140426, <https://doi.org/10.1098/rsta.2014.0426>, URL  
743 <https://royalsocietypublishing.org/doi/10.1098/rsta.2014.0426>, publisher: Royal Society.
- 744 Sutton, R. T., 2019: Climate Science Needs to Take Risk Assessment Much More Seri-  
745 ously. *Bulletin of the American Meteorological Society*, **100 (9)**, 1637–1642, [https://doi.org/](https://doi.org/10.1175/BAMS-D-18-0280.1)  
746 [10.1175/BAMS-D-18-0280.1](https://doi.org/10.1175/BAMS-D-18-0280.1), URL [https://journals.ametsoc.org/view/journals/bams/100/9/](https://journals.ametsoc.org/view/journals/bams/100/9/bams-d-18-0280.1.xml)  
747 [bams-d-18-0280.1.xml](https://journals.ametsoc.org/view/journals/bams/100/9/bams-d-18-0280.1.xml), publisher: American Meteorological Society Section: Bulletin of the  
748 American Meteorological Society.
- 749 Taylor, K. E., R. J. Stouffer, and G. A. Meehl, 2012: An Overview of CMIP5 and the Experiment De-  
750 sign. *Bulletin of the American Meteorological Society*, **93 (4)**, 485–498, [https://doi.org/10.1175/](https://doi.org/10.1175/BAMS-D-11-00094.1)  
751 [BAMS-D-11-00094.1](https://doi.org/10.1175/BAMS-D-11-00094.1), URL <https://journals.ametsoc.org/doi/10.1175/BAMS-D-11-00094.1>.
- 752 Tebaldi, C., and J. M. Arblaster, 2014: Pattern scaling: Its strengths and limitations, and an  
753 update on the latest model simulations. *Climatic Change*, **122 (3)**, 459–471, [https://doi.org/](https://doi.org/10.1007/s10584-013-1032-9)  
754 [10.1007/s10584-013-1032-9](https://doi.org/10.1007/s10584-013-1032-9), URL <https://doi.org/10.1007/s10584-013-1032-9>.
- 755 Tebaldi, C., and R. Knutti, 2007: The use of the multi-model ensemble in probabilistic climate  
756 projections. *Philosophical Transactions of the Royal Society A: Mathematical, Physical and*  
757 *Engineering Sciences*, **365 (1857)**, 2053–2075, <https://doi.org/10.1098/rsta.2007.2076>, URL  
758 <https://royalsocietypublishing.org/doi/10.1098/rsta.2007.2076>, publisher: Royal Society.
- 759 Tokarska, K. B., M. B. Stolpe, S. Sippel, E. M. Fischer, C. J. Smith, F. Lehner, and R. Knutti,  
760 2020: Past warming trend constrains future warming in CMIP6 models. *Science Advances*,  
761 **6 (12)**, eaaz9549, <https://doi.org/10.1126/sciadv.aaz9549>, URL [https://advances.sciencemag.](https://advances.sciencemag.org/content/6/12/eaaz9549)  
762 [org/content/6/12/eaaz9549](https://advances.sciencemag.org/content/6/12/eaaz9549), publisher: American Association for the Advancement of Science  
763 Section: Research Article.
- 764 Trenberth, K. E., and J. T. Fasullo, 2013: An apparent hiatus in global warm-  
765 ing? *Earth's Future*, **1 (1)**, 19–32, <https://doi.org/10.1002/2013EF000165>, URL  
766 <https://agupubs.onlinelibrary.wiley.com/doi/abs/10.1002/2013EF000165>, [\\_eprint:](#)  
767 <https://agupubs.onlinelibrary.wiley.com/doi/pdf/10.1002/2013EF000165>.

768 Viner, D., M. Ekstrom, M. Hulbert, N. K. Warner, A. Wreford, and Z. Zommers, 2020:  
769 Understanding the dynamic nature of risk in climate change assessments—A new start-  
770 ing point for discussion. *Atmospheric Science Letters*, **21** (4), e958, <https://doi.org/https://doi.org/10.1002/asl.958>, URL <https://rmets.onlinelibrary.wiley.com/doi/abs/10.1002/asl.958>,  
771 [\\_eprint: https://rmets.onlinelibrary.wiley.com/doi/pdf/10.1002/asl.958](https://rmets.onlinelibrary.wiley.com/doi/pdf/10.1002/asl.958),  
772

773 Zappa, G., 2019: Regional Climate Impacts of Future Changes in the Mid–Latitude Atmospheric  
774 Circulation: a Storyline View. *Current Climate Change Reports*, **5** (4), 358–371, <https://doi.org/10.1007/s40641-019-00146-7>, URL <https://doi.org/10.1007/s40641-019-00146-7>.  
775

## Supplementary Files

This is a list of supplementary files associated with this preprint. Click to download.

- [jclimcontraintesSI.pdf](#)